

Review of manuscript gchron-2022-1:

“Cosmogenic ^3He paleothermometry on post-LGM glacial bedrock within the central European Alps”

by N. Gribenski et al.

Comments by reviewer Samuel Niedermann

General comment

The authors have measured cosmogenic ^3He in quartz from two Alpine altitude profiles, with the aim to study paleo-temperature conditions in these areas that were gradually deglaciated after the LGM. They did the diffusion experiments that are required for a correct interpretation of the data and applied a lot of care in devising their experiments and model calculations, but obtained results that are difficult to interpret because temperatures recorded by cosmogenic ^3He are generally lower than expected based on the models. They discuss possible explanations for the discrepancy, but cannot give a final answer. Nevertheless, I think this is an important paper as it shows the difficulties (but also the potentials) involved in the rather new cosmogenic ^3He paleothermometry method and may thus prevent other scientists from misinterpreting their own data. With regard to the methods used, there is one thing that was not optimal in my opinion: Obviously, the helium analyses were confined to ^3He (at least nothing else is reported). Measuring ^4He also would have revealed any possible contributions of nucleogenic ^3He , which may lead to an overestimation of cosmogenic ^3He as argued in more detail below.

For the most part, the paper is written clearly and concisely. The English is generally fine, but suffers from quite a lot of small minor defects such as missing articles etc., which is a bit annoying given the fact that at least three co-authors are native English speakers. I have tried to point these out in the manuscript. Anyway, I recommend this manuscript for publication in *Geochronology* after minor revision has taken account of the specific and technical comments given hereafter.

Specific comments:

- In lines 172-182, the authors briefly describe the methods used for ^3He determination. Surprisingly for me, they don't mention anything about ^4He , and because there are no ^4He or $^3\text{He}/^4\text{He}$ data in the tables either, I assume they have not even checked for ^4He concentrations (otherwise those data should be given). This is a pity in the context of the discussion that many samples seem to contain more cosmogenic ^3He than expected (see below).
- Line 177: Why were blanks (only) measured at room temperature? Did you ever check whether they remain the same at higher temperatures up to the level used in the experiments? Otherwise that assumption seems a bit optimistic.
- In lines 523-537 the authors discuss a possible contribution of nucleogenic ^3He in the samples that has not been accounted for. They conclude that it “does not contribute significantly”, but their arguments are not very convincing because they have (obviously) not measured ^4He . It is known that purely radiogenic/nucleogenic He is characterized by typical $^3\text{He}/^4\text{He}$ ratios of $\sim(2\pm 2)\times 10^{-8}$. Thus, if the measured $^3\text{He}/^4\text{He}$ ratios in their

samples were on the order of 10^{-6} for example, the nucleogenic ^3He would be in the percent range at most and could safely be neglected. In my lab, I have measured several samples from similar settings (Mont Blanc area as well; work in progress) using two extraction steps of 600°C and 1000°C . While the 1000°C steps showed ratios in the 10^{-8} range as expected for radiogenic/nucleogenic He, the ratios in the 600°C steps varied from $\sim 6 \times 10^{-8}$ to several times 10^{-6} , implying that the nucleogenic ^3He contribution is not always negligible even in the low temperature step. Since the authors used 800°C as the first heating step, this is even more relevant for their samples. Their arguments for negligible nucleogenic ^3He are not very powerful. Assuming the same diffusion characteristics for nucleogenic and cosmogenic ^3He is probably not valid, since nucleogenic He is produced at different places in the minerals (namely, where Li is found, which is probably concentrated in mineral or fluid inclusions rather than in the quartz crystal itself). The fact that nucleogenic He is still degassed above 600°C while cosmogenic He is not shows on its own that the diffusion characteristics are different. Also, comparing the production rates of cosmogenic and nucleogenic He is not meaningful at all, since nucleogenic He has been produced over many millions of years, compared to the ~ 10 ka production of cosmogenic He. I don't say that the overabundance of cosmogenic ^3He in the authors' samples is indeed due to nucleogenic ^3He , but because of the lack of ^4He data it is difficult to rule it out.

Technical comments: (numbers refer to line numbers in the manuscript)

- 5-10 Please give zip codes of European cities before the city name (without comma), as customary here.
 - 19 Should be "... in quartz from the Mont Blanc site and and complex Arrhenius behavior in quartz from the Aar site...", as "behavior observed from the Aar site" is an odd wording.
 - 31 Tremblay et al. 2014a or 2014b?
 - 57 It is odd to say "glaciers retreated quickly behind the Little Ice Age moraines" when considering a time long before these moraines were there! Change to something like "behind the position were today the Little Ice Age moraines are located".
 - 64 I assume this should rather read "High-resolution $\delta^{18}\text{O}$ in Alpine speleothems ..."
 - 70 "which resulted in ... North Atlantic atmosphere patterns"??? Do you mean in variable atmosphere patterns? Then you should repeat that word (it's in singular in the first part, so it doesn't seem to belong to the plural term in the second one).
 - 77 There is no Bartlein et al. 2014 in the reference list (only B. et al. 2010).
 - 79 Please explain ELA for those readers who are not familiar with that term.
 - 132 "from the exact same locations previously collected" seems to imply you sampled surfaces from which some rock had already been knocked off before, i.e your surfaces would have been covered until a few years ago. I'm sure that's not what you did, but please clarify it!
- Fig. 2: On the y axis labels, remove dot after m because the symbol m for meter is never written with a dot. In the caption, it is confusing to write (a-c), (b-d) which seems to mean a to c and b to d, while obviously a and c, b and d is meant. So change to (a, c), (b, d).

Table 1: Lehmann et al. 2019 and Borchers et al. 2016 are not found in the reference list (but L. et al. 2020, B. et al. 2015). Give details about the method to estimate Mean Annual Rock Surface Temperatures. Please explain EDT or, at least, refer to the text section where it is explained.

184 Tremblay et al. (2021): Only Tremblay (2021) in reference list.

191 Is this the spallogenic or total ^{10}Be production rate?

192 Borchers et al. 2016 see above (Table 2)

243 What is “0.5 increment”? Do you mean increments of 0.5 kJ/mol? If so, you must give the unit!

244 Baxter et al. 2010 is not in reference list (only Baxter 2010).

Fig. 3: I can't see any gray lines, just gray areas between red and blue lines! This whole figure is very confusing and difficult to decipher, and the explanations in the caption do not help a lot. I ask the authors to think about how this figure could be improved, e.g. by showing several panels per location, and how it could be explained better.

284 Related to the above, I don't understand how the parameters E_a and $\ln(D_0/a^2)$ can be obtained from Fig. 3.

Table 2: 4th column from left, MBTP d3: Range 8.67 to 10, is that 8.67 to 10.00? If so, don't omit the .00, because otherwise it looks like this value was much less precisely determined than the other ones.

Fig. 4: At such a limited range of values (~2000-20,000), I don't see why a logarithmic scale is used for the y axis.

341-342 I assume what you mean is “... from the highest sample (...) partially overlaps that from MBTP18-9 within uncertainty.”

Fig. 5: What is the difference between the solid and dashed green lines in panels e and f?

374 Instead of “experiments”, which may imply something physical, better write “model runs” or similar.

487 Prud'Homme or Prud'homme as spelled in reference list?

514 Feldspar is not a mineral that is retentive for ^3He ; actually it is even less retentive than quartz! I don't think Masarik and Reedy have based their numbers on feldspar.

533 Farley et al. 2006 is not in reference list.

547 Liu et al. 2021 is not in reference list.

557 Berger and York 1981 is not in reference list.

596, 601 Baxter et al. 2010 is not in reference list (only Baxter 2010).

Data supplementary:

Fig. S1 Please use consistent sample labels throughout the manuscript. Here, GELM18-1 and GELM18-6 is written in the legend but GELM18-01, -06 in the figure caption.

Tab. S1, S2: The uncertainties given for ^3He are unrealistically small, in some cases <1 permil! This is obviously nonsense, no mass spectrometer is able to measure as precisely as that. I assume the authors only considered the statistical error of the measurement, disregarding other error sources such as mass spectrometer sensitivity or linearity. Even if the systematic errors (such as the uncertainty of the He concentration

in the standard that is used for sensitivity determination) are not taken into account, which makes sense in such a step-heating experiment (but should be noted), short-term variations of the sensitivity or deviations from the calibrated or assumed linearity of the mass spectrometer signal will be in the percent rather than the permil range.

Tab. S3: Similar to the ^3He uncertainties in Tab. S1 and S2, here the ^{10}Be uncertainties in the permil range are unrealistic. Again, it looks like only the $^{10}\text{Be}/^9\text{Be}$ measurement error was taken into account, without considering the uncertainty of the standard or carrier for example.

Footnote 2 should refer to Table S4 rather than Table S2.

Tab. S3, S4: In sharp discrepancy from the former two tables, ^3He errors are very high (on the order of 10%) here. While this may be realistic, the reason for the much higher uncertainties should be explained even when those in Tables S1 and S2 have been adjusted to a more realistic level.

The ^3He concentrations and their uncertainties are given with unreasonable precision, i.e. 6 significant digits for the errors. It is inappropriate (and confusing) to give more than two significant digits for an uncertainty, because uncertainties are not precise numbers but just represent probabilities. Therefore, values such as 520,929 should be rounded to 520,000, and of course the corresponding values should always be given with the same precision as the uncertainties. The first entry in Table S3 would thus be $6,400,000 \pm 520,000$, or better readable (and easier to round in Excel, e.g.) 6.40 ± 0.52 in units of 10^6 at/g.

I wonder how the average values from the three replicate measurements were calculated. For three measurements agreeing within error limits, as seems to be the case looking at Table S4, an error-weighted mean could be calculated. Obviously, the authors calculated an unweighted average instead and, very strangely, used the average of the errors as the error of the average. I don't think this is a statistically correct way.



Cosmogenic ^3He paleothermometry on post-LGM glacial bedrock within the central European Alps

Natacha Gribenski^{1,2}, Marissa M. Tremblay³, Pierre G. Valla⁴, Greg Balco⁵, Benny Guralnik⁶, David L. Shuster^{5,7}

5 ¹Institute of Geological Sciences, University of Bern, Bern, 3012, Switzerland

²Oeschger Centre for Climate Change Research, University of Bern, Bern, 3012, Switzerland

³Department of Earth, Atmospheric, and Planetary Sciences, Purdue University, West Lafayette, IN 47901, USA

⁴University Grenoble Alpes, University Savoie Mont Blanc, CNRS, IRD, IFSTTAR, ISTERre, Grenoble, 38000, France

⁵Berkeley Geochronology Center, Berkeley, CA 94709, USA

10 ⁶Technical University of Denmark, Kgs. Lyngby, 2800, Denmark

⁷Department of Earth and Planetary Science, University of California, Berkeley, CA 94709, USA

Correspondence to: Natacha Gribenski (natacha.gribenski@geo.unibe.ch)

Abstract. Diffusion properties of cosmogenic ^3He in quartz at Earth's surface temperatures offer the potential to reconstruct the evolution of past in-situ temperatures directly from formerly glaciated areas, information important for improving our understanding of glacier-climate interactions. In this study, we apply cosmogenic ^3He paleothermometry on rock surfaces gradually exposed since the Last Glacial Maximum (LGM) to the Holocene period along two deglaciation profiles in the European Alps (Mont Blanc and Aar massifs). Laboratory experiments conducted on one representative sample per site indicate significant variability in ^3He diffusion kinetics between the two sites, with quasi linear Arrhenius behavior observed in quartz from the Mont Blanc site and complex Arrhenius behavior observed from the Aar site, which we interpret to indicate the presence of multiple diffusion domains (MDD). Assuming that the same diffusion kinetics apply to all quartz samples along each profile, predictive simulations indicate that ^3He abundance in all the investigated samples should be at equilibrium with present-day temperature conditions. However, measured natural ^3He concentrations in samples exposed since before the Holocene indicate an apparent ^3He thermal signal significantly colder than today. This observed ^3He thermal signal cannot be explained with a realistic post-LGM mean annual temperature evolution in the European Alps at the study sites. One hypothesis is that the diffusion kinetics and MDD model applied may not provide sufficiently accurate, quantitative paleo-temperature estimates in these samples; thus, where pre-Holocene ^3He thermal signal is indeed preserved in the quartz, the helium diffusivity would be lower at Alpine surface temperatures than our diffusion models predict. Alternatively, if the modeled helium diffusion kinetics is accurate, the observed ^3He abundances may reflect complex geomorphic/paleoclimatic evolution with much more recent ground temperature changes associated with the degradation of alpine permafrost.



30 1 Introduction

This study applies cosmogenic noble gas paleothermometry (Tremblay et al., 2014) to attempt to reconstruct temperature changes associated with gradual ice lowering following the Last Glacial Maximum (LGM ca. 27-19 ka; Clark et al., 2009) in two sites of the high European Alps. Because glaciers are sensitive to both temperature and precipitation, obtaining information about *in situ* temperature conditions from an independent proxy is critical to disentangling the role of either variable in recorded
35 glaciers fluctuations and to adequately use these records for paleoclimate reconstructions. In particular, paleoglacier records can then be used as direct site-specific paleo-precipitation indicators (e.g., Kerschner et al., 2000; Kerschner and Ivy-Ochs, 2008; Martin et al., 2020) to trace changes in regional atmospheric circulation systems (Kuhlemann et al., 2008; Becker et al., 2016; Gribenski et al., 2021). More detailed information about paleoclimate conditions would moreover improve our understanding of glacier response(s) to current climate change as well as our ability to anticipate glacier evolutions for
40 proposed future climate scenarios (Zemp et al., 2006; Haeberli et al., 2020). Furthermore, direct temperature constraints associated with paleoglacier variations are also critical to our understanding of glacier erosion processes (Hallet, 1970) which have profoundly shaped high-latitude and mountain landscapes over 10^3 to 10^6 yr timescales (Herman et al., 2021), and which
s to relate, among other factors, to climatic conditions (Koppes et al., 2015; Cook et al., 2020).

Available data on the relationship between glacier geometry and climate as well as between glacial erosion and climate are
45 largely biased toward present-day and historical time periods, therefore obliging us to rely on the assumption that modern to centennial records are representative of the range of variation and mechanistic trends between climate/glacier variation and erosion operating on geological time scales (Jaeger and Koppes, 2016). While combined records of paleoglacier geometry and erosion rates on Late-Pleistocene timescales are growing thanks to the recent development of analytical and numerical techniques (e.g., Kapannusch et al., 2020; Mariotti et al., 2021), obtaining direct quantitative paleoclimate constraints from
50 formerly glaciated areas remains challenging, even for regions with relatively well known paleoglacial histories. In the European Alps, the most detailed paleoglacier record goes back to the Late Pleistocene ice maximum advance, dated around ~26-24 ka in the northern and central Alps (Monegato et al., 2017), in line with the global LGM. During the LGM, ice spread to within several tens of kilometers of the piedmonts and reached more than 1000-1500 m thick in the main valleys (Ivy-Ochs, 2015; Wirsig et al., 2016a). More restricted stages (i.e., Gschnitz, Daun, Egesen stadials; Ivy-Ochs, 2015) marking the gradual
55 retreat (and thinning) of the ice into the upper catchments followed between the LGM and the Younger Dryas cooling event (YD, 12.8-11.7 ka; Heiri et al., 2014a). During the early Holocene (i.e., the last 11 ka; Heiri et al., 2014a), glaciers retreated quickly behind the Little Ice Age moraines, and remained within these limits for the rest of the Holocene period (Heiri et al., 2014a).

The recorded Alpine glacial sequence is consistent with polar ice oxygen isotope ($\delta^{18}\text{O}$) records from the Northern hemisphere
60 (NGRIP, 2004), which indicate temperature minima reached at 25-20 ka (around a -20°C anomaly in central Greenland compared to present mean annual temperatures), followed by a gradual increase until ca. 10 ka with the last pronounced isotopic excursion at ca. 12 ka (YD event, around -15°C anomaly; Buizert et al., 2018). After the YD, temperatures stabilized



around values similar to today with only minor fluctuations (less than 2°C) throughout the remaining Holocene period (Buizert et al., 2018). High-resolution Alpine $\delta^{18}\text{O}$ speleothems similarly support a coupling between the northern European Alps and
65 Greenland records (Moseley et al., 2020; Li et al., 2021).

While there is evidence for temporal coupling, a direct (scaled) translation of polar ice records over the Alps to obtain quantitative temperature/precipitation constraints is inappropriate. Indeed, major climate forcing components (i.e., ice sheet, atmospheric greenhouse gas and ocean circulation) also underwent large-scale changes between the LGM and the Holocene transition (Clark et al., 2012), which resulted in a variable pre-Holocene latitudinal temperature gradient (Heiri et al., 2014b)
70 and North Atlantic atmospheric patterns (Eynaud et al., 2009). Existing past climate information from Alpine paleoenvironmental proxies is mainly qualitative with only a few scarce and fragmented quantitative temperature/precipitation records available for the pre-Holocene period (Heiri et al., 2014a). These are mostly from proxies located on the outer rim of the Alpine range from lake and peat archives (e.g., pollen, chironomids; Heiri et al., 2014a) and groundwater and speleothems (i.e., noble gas; Beyerle et al., 1998; Ghadiri et al., 2018) or tentatively-derived from inverse glacial modeling (Kerschner and
75 Ivy-Ochs, 2008; Becker et al., 2016; Seguinot et al., 2018), with some noticeable variability in derived paleoclimate information between and within proxies records. Proposed reconstructed mean temperature anomalies during the LGM hence vary from -11 to -14°C based on pollen reconstructions (Wu et al., 2007; Bartlein et al., 2014), -5 to -9°C based on noble-gas groundwater records (Beyerle et al., 1998, Seltzer et al., 2021), and -8 to -15 °C using glacial modeling studies calibrated on reconstructed ice limits and paleo-ELA estimates (Allen et al., 2008; Becker et al., 2016; Seguinot et al., 2018; Vukobratovic et al., 2020). LGM precipitation conditions are even more uncertain, with estimates for precipitation anomalies varying widely
80 (around -20 to -60%; e.g., Peyron et al., 1998; Luetscher et al., 2015; Becker et al., 2016), and for which a differential north-south distribution pattern (Florineth and Schuster, 2000; Becker et al., 2016; Luetscher et al., 2015) is still debated (Seguinot et al., 2018; Vukobratovic et al., 2020). Similarly, little is known regarding climatic conditions between the LGM and the YD, besides that significantly lower (>6°C negative anomalies) summer temperatures were still persisting before ca. 15 ka, based
85 on chironomid and treeline proxies (Heiri et al., 2014a). During the short lived (~1 kyr) YD cooling event, temperatures dropped, with mean annual anomalies varying between 2-3 to 5-9 °C below present day values, depending on the considered proxy between paleoglacial reconstructions (e.g., Protin et al., 2019; Baroni et al., 2021), lacustrine pollen assemblages (Magny et al., 2001) and noble gas speleothem records (Ghadiri et al., 2018; Affolter et al., 2019). On the other hand, for the Holocene period, all the available records are in general agreement to indicate that temperatures conditions relatively similar to today
90 prevailed, with only minor (less than 2°C) deviations (e.g., Davis et al., 2003; Ghadiri et al., 2018; Affolter et al., 2019; Heiri et al., 2014a). Today, there is hence a crucial lack of direct and quantitative *in situ* temperature constraints from within the Alpine massifs during the different reconstructed glacial stages since the LGM.

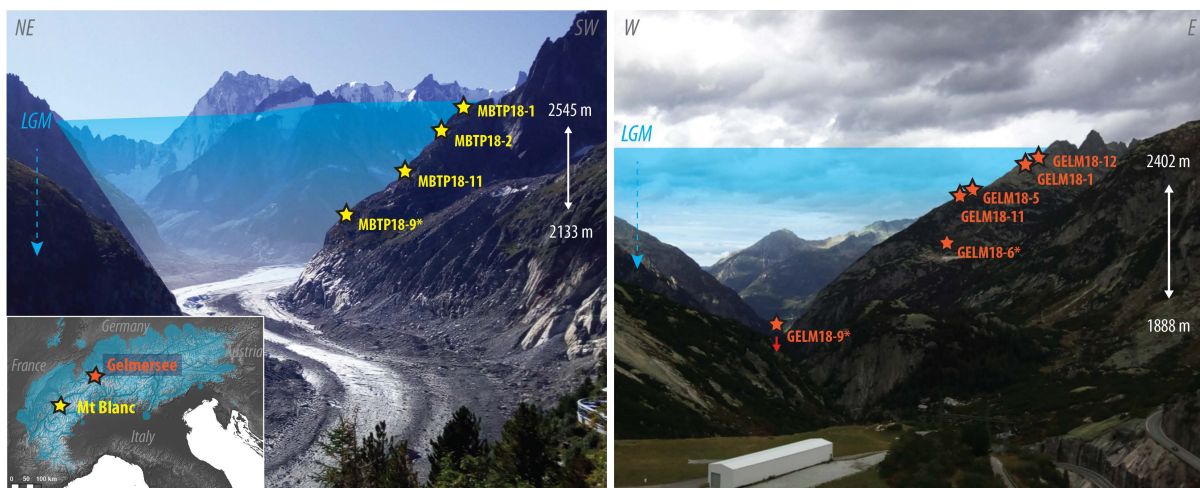
In this study, we attempt to reconstruct paleotemperatures in the high Alps between the LGM and YD (i.e., Late Glacial) by applying cosmogenic noble gas paleothermometry (Tremblay et al., 2014a). This method exploits the open-system behavior
95 of cosmogenic ^3He in quartz minerals at Earth surface temperatures (Brook et al., 1993; Shuster and Farley, 2005). Using predictive models of ^3He production and diffusion loss through time and temperature, quantitative constraints on the thermal

history of an exposed rock surface can thus be inferred from the difference between surface-exposure ages derived from the “leaky” ^3He system and from a cosmogenic nuclide that does not express open-system behavior (e.g., ^{10}Be), which records a surface-exposure duration assuming non-complex history (Tremblay et al., 2014a, b; 2018). Cosmogenic ^3He paleothermometry provides a unique opportunity to obtain quantitative information about past temperature from *in situ* rock surfaces located in the formerly glaciated Alps. Here we explore the applicability of cosmogenic ^3He paleothermometry along two deglaciation profiles in the northern and western Alps. The advantages of such sampling targets are (1) *a priori* relatively simple exposure history of rock surfaces revealed between the LGM and YD (Wirsig et al., 2016b; Lehmann et al., 2020) with limited shadowing effect (e.g., steep surface, limited vegetation or postglacial sediment cover) and (2) the access to sequences of gradually exposed but lithologically similar samples, enabling a semi-continuous record of a temperature-change history. Based on ^3He analytical measurements and forward simulation experiments, we aim to investigate the sensitivity of the *in situ* quartz- ^3He system in two different high Alpine areas and its suitability for the preservation of a ^3He thermal signal on Late-Pleistocene timescales. We also compare our results to previous studies applying cosmogenic ^3He paleothermometry elsewhere in the Alps to gain a further understanding of ^3He diffusion behavior in quartz at Earth surface temperatures.

2 Study sites and sample measurements

2.1 Settings and sample collection

Two sites located in major Alpine massifs were selected for this study and have been previously investigated for their deglaciation history: the Mont Blanc Trelaporte (MBTP) profile (Mont Blanc massif, France; Lehmann et al., 2020), located in the western Alps along the western flank of the Mer de Glace valley (NNE exposure); and the SW exposed Gelmersee (GELM) ridge (Aar massif, Switzerland; Wirsig et al., 2016b), formed by a hanging valley on the east wall of the Haslital valley, in the northern central Alps (Fig. 1, inset). Both sites have steep valley sides that are several hundred meters high with $\sim 30\text{-}35^\circ$ slopes, and are characterized by smoothly-abraded rock surfaces and “roche moutonnée”-like features molded by flowing glaciers. Homogeneous lithologies are exposed along the valley walls, with phenocrystalline granite of the Mont Blanc (Dobmeier, 1998) at the MBTP site, and Aare granite (Labhart, 1977; Abrecht, 1994) as part of the Helvetic crystalline basement at the GELM site. At both sites, the upper parts of the valley sides are characterized by jagged rock surfaces resulting from active periglacial processes. The transition between smooth and rough surfaces (i.e., the trimline), located at ~ 2600 a.s.l. at the MBTP site and ~ 2450 a.s.l. at the GELM site, either marks the upper limit of the LGM ice surface or of the active (warm-based) eroding glacier layer (i.e., subglacial boundary; Wirsig et al., 2016a).



125 **Figure 1: Mont Blanc Trelaporte (MBTP, left) and Gelmersee (GELM, right) deglaciation profiles since the Last Glacial Maximum (LGM), with the spatial distribution of samples collected for quartz ^{10}Be (Lehmann et al., 2020; Wirsig et al., 2016b) and ^3He (this study) analyses. Samples with an asterisk have been exposed for ~10-11 kyr (i.e., the entire Holocene period). The inset map indicates the location of the two study sites within the European Alps and the extent of ice cover during the LGM (in blue; Ehlers et al., 2011).**

Ice-surface lowering of around 400 (MBTP) to >500 (GELM) meters between the LGM to the YD has been recorded using *in situ* ^{10}Be cosmogenic exposure dating on bedrock surfaces collected at regular intervals along each profile, starting from just below the trimline (Figs. 1-2, Table 1; Lehmann et al., 2020; Wirsig et al., 2016b). In this study, samples were collected again for ^3He experiments from the exact same locations previously collected for ^{10}Be dating by Lehmann et al. (2020; MBTP profile, samples MBTP18 -1, -2, -11 and -9, n=4) and Wirsig et al. (2016b; GELM profile, samples GELM18 -12, -1, -5, -11, -6 and -9, n=6; Fig. 1, Table 1). All samples are from glacially scoured bedrock surfaces, except GELM18-11, which comes from the top of a ~5-m high boulder of similar lithology deposited during the post-LGM ice-surface lowering (Wirsig et al., 2016b).

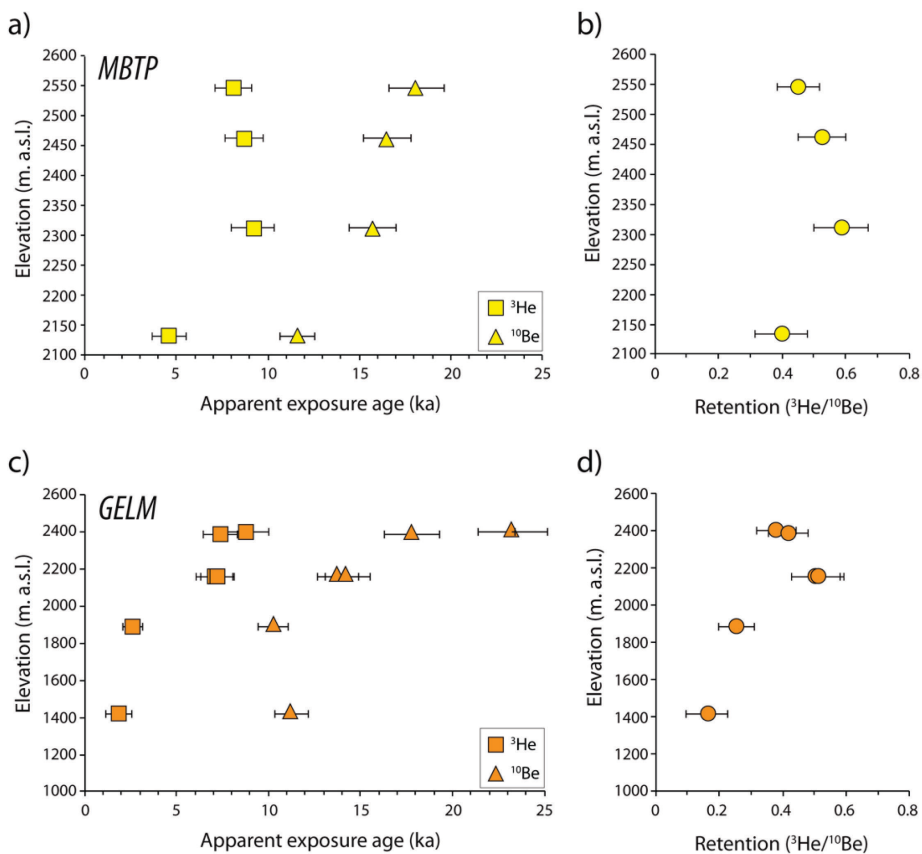


Figure 2: Apparent ^3He (this study) and ^{10}Be (Lehmann et al., 2020; Wirsig et al., 2019) exposure ages (a-c), and $^3\text{He}/^{10}\text{Be}$ exposure age ratios or retention (b-d) as a function of elevation along the two deglaciation profiles (MBTP: a-b; GELM: c-d).

140 Table 1: MBTP and GELM sample information.

Profile	Sample	Lat./Long. (°N/°E)	Alt. (asl)	^{10}Be age (ka) ²	^3He age (ka) ²	MARST (°C) ³	Modern EDT (°C) ⁴	Paleo IsoEDT (°C)
MBTP	MBTP18-1	45.9083/6.9311	2465	18.1±1.5	8.1±1.0	1.2	5.8	3±1.5
	MBTP18-2	45.9086/6.9319	2460	16.5±1.3	8.7±1.0	1.7	6.2	0.5±2
	MBTP18-9 ¹	45.9124/6.933	2133	11.6±1.0	4.6±0.9	2.4	8.0	8±2.5
	MBTP18-11	45.9108/6.9315	2310	15.7±1.3	9.2±1.1	3.3	7.0	-1.5±2.5
GELM	GELM18-1 ¹	46.6218/8.3257	2387	17.8±1.5	7.4±0.9	3.1	7.9	-5.5±3
	GELM18-5	46.6185/8.3215	2155	13.8±1.1	7.0±1.0	4.3	9.1	-11±3
	GELM18-6	46.6151/8.3212	1888	10.2±0.8	2.6±0.5	5.7	10.6	9.5±3
	GELM18-9	46.6136/8.3071	1418	11.2±0.9	1.8±0.7	8.1	13.1	14.5±4
	GELM18-11	46.618/8.3217	2154	14.3±1.2	7.2±0.9	4.3	9.1	-11±3
	GELM18-12	46.6221/8.3258	2402	23.3±1.9	8.8±1.2	3.0	7.8	-4.5±3

¹Samples used for ^3He diffusion experiments. ²Re-calculated ^{10}Be (after Wirsig et al., 2019 and Lehmann et al., 2019) and calculated ^3He exposure ages using the non-time dependent scaling scheme of Stone (2000; Balco et al., 2008), using SLHL production rates of

145 4.01 $\text{at.g}^{-1}.\text{yr}^{-1}$ (^{10}Be ; Borchers et al., 2016) and of 116 $\text{at.g}^{-1}.\text{yr}^{-1}$ (^3He ; Vermeesch et al., 2009) and assuming a rock density of 2.65 g.cm^{-3} . See the supplementary material for the details of ^{10}Be and ^3He concentrations (Table S3). $^3\text{Estimated Mean Annual Rock Surface Temperature at } \sim 3 \text{ cm depth. } ^4\text{Modern EDTs calculated using } E_a \text{ of } 93.5 \text{ (MBTP) or } 98.5 \text{ (GELM) kJ.mol}^{-1}$, $^5\text{Samples specific MARST estimates and using } 10^\circ\text{C annual and } 5^\circ\text{C diurnal amplitudes.}$

2.2 Samples preparation and measurement experiments

150 Aside from the exposure time of a rock surface determined using independent chronometers (in our case *in situ* ^{10}Be surface-exposure dating), cosmogenic ^3He paleothermometry requires at least two additional pieces of information. First, predictive models of thermally-activated ^3He diffusion rely on quartz sample-specific ^3He diffusion kinetics parameters (i.e., activation energy E_a and the diffusion at infinite temperature scaled to the diffusion length scale (pre-exponential factor) D_0/a^2 ; Tremblay et al., 2014a, b), which need to be experimentally determined. Second, measurement of the total natural cosmogenic ^3He accumulated in the quartz sample permits us to estimate the loss by diffusion which occurred throughout the exposure time of the rock surface.

155 Rock samples were disaggregated using a high-voltage pulse-based system (SELFRAG equipment, Institute of Geological Sciences, University of Bern) to optimize the breaking of the rock along crystal grain boundaries. After rinsing, quartz mineral grains were separated from the other minerals (heavy minerals and feldspar) by magnetic separation and froth flotation (e.g., Nichols and Goehring, 2019) and were additionally etched in 1% HF for 3 weeks at room temperature to ensure the removal of any adhesive micro-mineral particles which may contaminate the ^3He measurements. For both sites, grain-size distribution after removal of the finer fraction ($<200 \mu\text{m}$) is centered around 850 μm diameter (Fig. S1). One representative sample per profile was selected for diffusion kinetics experiments (MBTP18-9 and GELM18-1). For these samples, 200 to 300 mg of quartz grains were visually selected under a binocular microscope to avoid obvious mineral inclusions and sent to the Francis H. Burr Proton Therapy Center (Massachusetts General Hospital) for proton beam irradiation (Shuster et al., 2004; Shuster and Farley, 2005) in February 2019. After several months of rest to lower the level of radioactivity, one individual coarse quartz grain ($\sim 700 \mu\text{m}$ diameter for MBTP18-9 and $\sim 900 \mu\text{m}$ diameter for GELM18-1, based on calibrated petrographic microscope measurements) with no obvious fractures and no mineral or fluid inclusion was selected from each irradiated sample to conduct step-degassing experiments. For natural ^3He measurements, the 800-1000 μm quartz grain fraction (i.e., 400-500 μm radii) from each sample was isolated, as we anticipated this fraction would have best preservation potential of a measurable ^3He signal for the expected range of thermal histories experienced by the MBTP and GELM samples (Brook and Kurz, 1993; Tremblay et al., 2014a). Three replicates per sample were prepared in tantalum packets containing $\sim 100 \text{ mg}$ of quartz grains for analysis of natural ^3He concentrations.

175 Both stepwise-heating experiments to characterize the ^3He diffusion kinetics in the proton-irradiated quartz grains and bulk degassing measurements to determine the natural cosmogenic ^3He abundances in the $\sim 100 \text{ mg}$ quartz grain replicates were carried out at the BGC Noble Gas Thermochronometry Lab (Berkeley, USA). The measurements were conducted with an MAP 215-50 sector field mass spectrometer following a similar procedure to Tremblay et al. (2014b). For diffusion kinetics experiments, samples were heated over thirty to forty heating steps lasting 0.5 to 4 hours, with temperatures increased from



100 up to 550°C and including at least one retrograde heating cycle (Tables S1-S2). Blank measurements at room temperature were regularly conducted throughout the experiments for background subtraction from the measured raw signals, with averaged ^3He blank corrections of 2.1×10^4 atoms (MBTP18-9) and 4.9×10^4 atoms (GELM18-1). For natural cosmogenic ^3He measurements (Tables S3-S4), each tantalum packet was heated in two, 15-minute long heating steps at 800 and 1100 °C, with no gas release observed in the second step. Hot blanks on empty tantalum packets were measured, from which an averaged ^3He blank correction of 7.7×10^3 atoms was applied.

3 Analytics approach: constraining diffusion kinetics and Effective Diffusion Temperature

In this study, we used Matlab codes initially developed by Tremblay et al. (2014a, b; 2018; 2021, code available on Zenodo at <https://doi.org/10.5281/zenodo.5808021>) to (1) determine ^3He diffusion kinetics from step-heating experiment data applying a multi-diffusion domain (MDD; Lovera et al., 1989, 1991) model framework, and (2) numerically simulate ^3He loss for different thermal histories using the sample-specific diffusion kinetics information. The predictive model of ^3He diffusion with time also includes ^3He production by cosmic ray incidence using a ^3He production rate in quartz at sea level and high latitude (SLHL) of $116 \text{ at.g}^{-1}.\text{yr}^{-1}$ (Vermeesch et al., 2009), scaled to the sample geographic location and elevation according to the non-time dependent scaling scheme of Stone (2000; Balco et al., 2008). For consistency, apparent ^3He and ^{10}Be exposure ages along the deglaciation profiles are (re-)calculated following the same approach (with SLHL ^{10}Be production rate of $4.01 \text{ at.g}^{-1}.\text{yr}^{-1}$; Borchers et al., 2016), using the measured ^3He (this study) and literature ^{10}Be concentrations (previous studies, Wirsig et al., 2016b; Lehmann et al., 2020), assuming negligible erosion (Fig. 2; Tables 1 and S3). Recalculated ^{10}Be exposure ages define the exposure time of sampled rock surfaces during which we simulate ^3He production and diffusion as a function of ambient temperature. In order to account for periodic temperature oscillations (e.g., diurnal, seasonal, geological), effective diffusion temperatures (EDTs, Tremblay et al., 2014a) are used as temperature inputs in the predictive ^3He diffusion model as detailed below.

3.1 Effective Diffusion Temperature estimates

Rock surfaces experience temperature fluctuations at the diurnal, seasonal and longer timescales, which will all activate thermal diffusion of ^3He in quartz (Tremblay et al., 2014a). Because ^3He diffusivity increases exponentially with temperature, a constant model temperature required to explain a total ^3He loss (i.e., corresponding to the mean diffusivity through time) from a geological sample will equal or exceed the actual mean temperature experienced at the rock surface. This temperature is called Effective Diffusion Temperature (EDT; Christodoulides et al., 1971; Tremblay et al., 2014a), and is a function of the ^3He diffusion activation energy E_a , the long-term mean (rock surface) temperature and the diurnal and seasonal temperature amplitudes.

In our approach, temperature variables used for the EDT calculation at the different sampling sites (which are subsequently used for ^3He diffusion simulations; cf. Sect. 3) were estimated as follows. Mean annual air temperatures (MAATs) at each



sampling sites along the MBTP and the GELM profiles were calculated by linear interpolation assuming a lapse rate of 5°C/km (Gruber et al., 2018) based on mean annual temperatures recorded by nearby reference weather stations at Chamonix (1042
210 m.a.s.l., ~5 km west; period 1993-2012; Magnin et al., 2015a) and Grimsel-Hospiz (1980 m.a.s.l.; ~5 km south; period 2010-
2020, data MeteoSwiss), respectively. Mean Annual Rock Surface Temperatures (MARSTs) are typically higher than MAATs,
with the difference amplified between south- and north-exposed slopes (Gruber et al., 2003). Boeckli et al. (2012a), based on
57 sensor measurements on snow-free rock slopes >55°, showed that the measured difference between MAAT and MARST
215 increased linearly from <1°C to up to 10°C depending on potential incoming solar radiation (PISR), which is largely controlled
by rock surface aspect and angle, in addition to elevation. For moderately inclined surfaces, the difference between MARST
and MAAT is expected to be reduced by ~1-3°C due to micro-topography and snow-insulating effects (Hasler et al., 2011).
To estimate MARSTs, we calculated the PISR at each sampling site using the Area Solar Radiation tool (ArcGIS software,
version 10.3.1) applied to a 30 m resolution Digital Elevation Model (SRTM 1 Arc-Second data) at the study sites. The
calculation was performed at hourly resolution using data from one year (2000), assuming no nebulosity and using a sky size
220 of 512 cells (Magnin et al., 2015a; Mair et al., 2020). Based on the linear relationship between MAAT-MARST and PISR
from Boeckli et al. (2012a), we estimated the average MARST-MAAT difference assuming snow-free conditions at each site,
which we then subtracted 2 °C to take into account snow-insulating and micro-topographic effects in moderately steep
terrain (Hasler et al., 2011). Final differences between MAAT and MARST of +1°C and +2.5°C were thus obtained for the
north-exposed MBTP and the southwest-exposed GELM sites, respectively. These estimates are consistent with *in situ* MAAT
225 and MARST measurements available in nearby areas with similar orientations, elevations and slope inclinations (e.g., Gruber
et al., 2004; Magnin et al., 2015a, b; Haberkorn et al., 2017; Gruber et al., 2018; Guralnik et al., 2018), and were thus used
to estimate the MARSTs at each sampling site.
A mean annual temperature amplitude of 10°C and diurnal amplitude of 5°C were adopted for the two sites, based on long-
term (i.e., several years) temperature records from the Chamonix and Grimsel-Hospiz weather stations, and from direct *in situ*
230 rock surface measurements available in the Alps (Gruber et al., 2004; Magnin et al., 2015b; Gruber et al., 2018; Mair et al.,
2020; Guralnik et al., 2018). These estimates are consistent with the annual/diurnal amplitudes obtained from the spatially-
interpolated land surface climate data set WorldClim 2.0, based on gridded time series of meteorological data from available
weather stations (target temporal range 1970-2000; 1 km resolution; Fick and Hijmans, 2017).

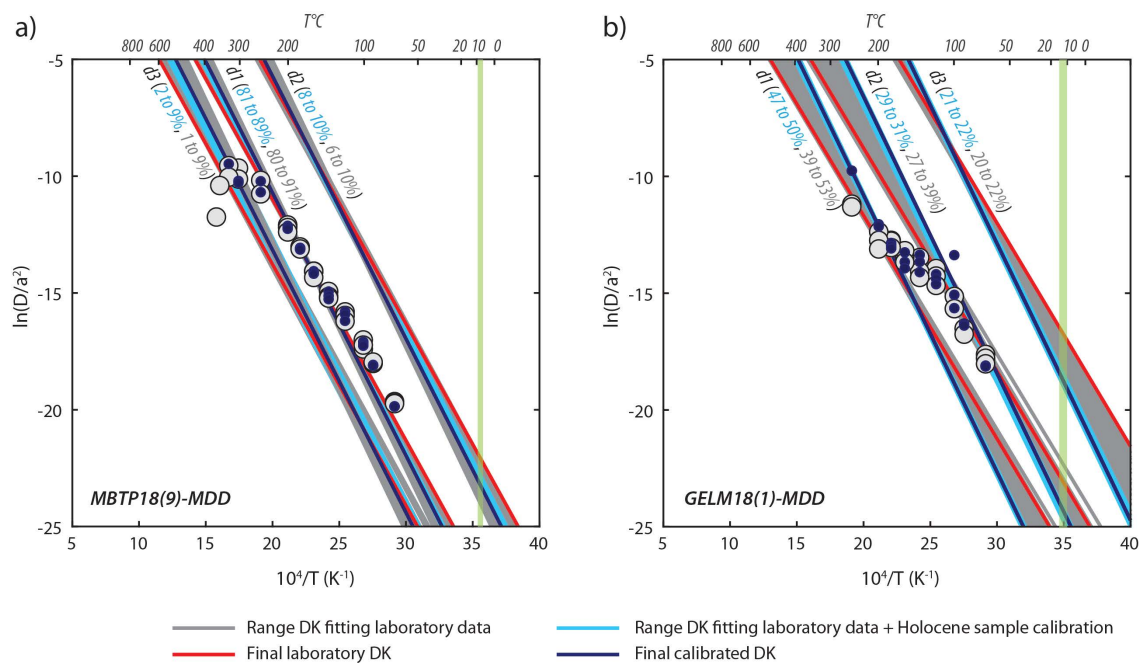
3.2 Diffusion kinetics determination

235 Diffusion kinetics parameters (E_a and $\ln(D_0/a^2)$) were determined following a multi-step procedure. For each proton-irradiated
sample (one per site), we first produced an Arrhenius plot displaying the natural log of diffusivity D (scaled to the diffusion
length scale a) as a function of inverse temperature (Fig. 3), calculated from each ^3He degassing step experiment using the
equation of Fechtig and Kalbitzer (1966; in Tremblay et al., 2014b).

Preliminary tests using the MDD model framework described by Tremblay et al. (2014b) were carried out to determine the E_a
240 required to best fit the Arrhenius data points in the lower temperature range (~70 to 100°C) assuming a single diffusion array,

as well as the (minimum) number of diffusion domains to explain the entire data set (i.e., all heating steps). Iterative experiments using the MDD model with the minimum number of domains inferred from the preliminary tests were then conducted for a range of increasing E_a up to 100 kJ/mol (with 0.5 increment; Fig. 3), based on existing E_a estimates reported for quartz in the literature (Tremblay et al., 2014b; Tremblay et al., 2018). In each experiment, E_a was kept common to each domain (Lovera et al., 1991; Baxter et al., 2010) while $\ln(D_0/a^2)$ and gas fraction were allowed to vary between the different domains until the misfit coefficient was minimized between the simulated and observed $\ln(D/a^2)$ values for all the heating steps.

Because heating step degassing experiments conducted in laboratory do not permit to capture ^3He diffusion behavior at Earth's surface temperature range (i.e., from around -30 to 30°C), we next introduced an extra calibration step using the measured natural ^3He concentration from the samples with Holocene-only exposure (from both GELM and MBTP sites) to constrain diffusion kinetics which might be more representative in the range of temperature conditions experienced by Alpine rock surfaces. Based on independent global and regional paleoclimate proxy records, samples exposed during the Holocene have experienced relatively stable averaged temperature conditions with only minor variations (i.e., less than 2°C ; cf. Sect. 1). Assuming no complex exposure history, the ^3He signal recorded in these samples can therefore be considered representative of ^3He diffusion occurring at a constant temperature equivalent to the EDT calculated at each sample site. We thus conducted another series of numerical experiments to test sets of diffusion kinetic parameters determined from our laboratory experiments that explain the natural ^3He concentrations recorded in the Holocene samples available in our two study sites (MBTP18-9, ^{10}Be exposure age of ca. 11.6 ka; GELM18-9 and-6, ^{10}Be exposure ages of ca. 10.2 and 11.2 ka). For each study site, the corresponding set of E_a and associated $\ln(D_0/a^2)$ per domain (with gas fraction) was thus implemented in the forward simulation model of ^3He evolution with time and temperature (Tremblay et al., 2014a), which was run over a time period equivalent to the recalculated ^{10}Be exposure age and for a constant temperature equivalent to the modern EDT (recalculated accordingly for each E_a , based on sample specific temperature variables, cf. Sect. 3.1.) of the Holocene sample(s). Diffusion kinetics parameters for which the resulting modeled ^3He concentration matched within error the observed natural one (i.e., from the Holocene sample considered) were retained, with the solution producing the best match considered as the final calibrated diffusion kinetics parameters (Fig. 3). We assume the Holocene-calibrated parameters apply to all the samples (i.e., including with longer exposure durations) collected along each profile (MBTP or GELM), given the homogenous lithology between samples, and were used as the default diffusion kinetics parameters for the numerical experiments conducted in the next sections.



270 **Figure 3:** Arrhenius plots of ^3He step-degassing experiments (grey circles) conducted on one representative sample per study site. Final diffusion kinetics parameters were determined using a multi-step procedure, including the determination of MDD diffusion kinetics (DK) parameters that (1) best fit the laboratory data for a range of increasing E_a (79 (a) and 86 (b) to 100 kJ/mol; grey lines; red lines show final laboratory parameters providing the best match in the lower temperature range), and (2) match within 275 uncertainties the natural ^3He concentration recorded in the Holocene calibration samples (light blue lines). The dark blue line indicates the final calibrated DK parameters best matching the step-degassing experiments and the natural Holocene ^3He concentration (dark dots represent the corresponding $\ln(D/a^2)$ values modeled along the heating experiment schedule). For the MBTP site (a), sample MBTP18-9 was used for both the laboratory step-degassing experiment as well as the Holocene calibrating sample. For the GELM site (b), sample GELM18-1 was used for the laboratory step-degassing experiment, while sample GELM18-6 and -9 were used for Holocene calibration. The light green line indicates the EDT range associated with the Holocene calibration sample(s). The gas fraction assigned to each domain for both laboratory (grey font) and Holocene-calibrated (blue font) DK 280 parameters is also indicated along lines.

4 Results

4.1 Diffusion kinetics and sensitivity tests

We present in Figure 3 the range of diffusion kinetics parameters (E_a and $\ln(D_0/a^2)$) fitting the laboratory degassing experiments (one representative sample for each site), and which in addition predict the observed natural ^3He concentrations from the Holocene calibration samples for a constant EDT equivalent to the modern EDT. Degassing experiment data indicate relatively 285 first-order Arrhenius behavior for quartz ^3He diffusion of MBTP18-9, with one dominant linear array accounting for ~85% of ^3He release (Fig. 3a, Table 2). The remaining ~15% gas fraction is distributed within two additional minor diffusion domains, one of higher retentivity and one of lower retentivity (Tremblay et al., 2014b). GELM18-1 exhibits more complex quartz ^3He diffusion behavior, with gas release distributed more equally (gas fraction between 20 290 50%) within three linear arrays (Fig.



3b, Table 2), which can be interpreted as three distinct diffusion domains with each domain contributing significantly to ³He retention over geological times.

Table 2: Diffusion kinetics parameters for MBTP and GELM sites.

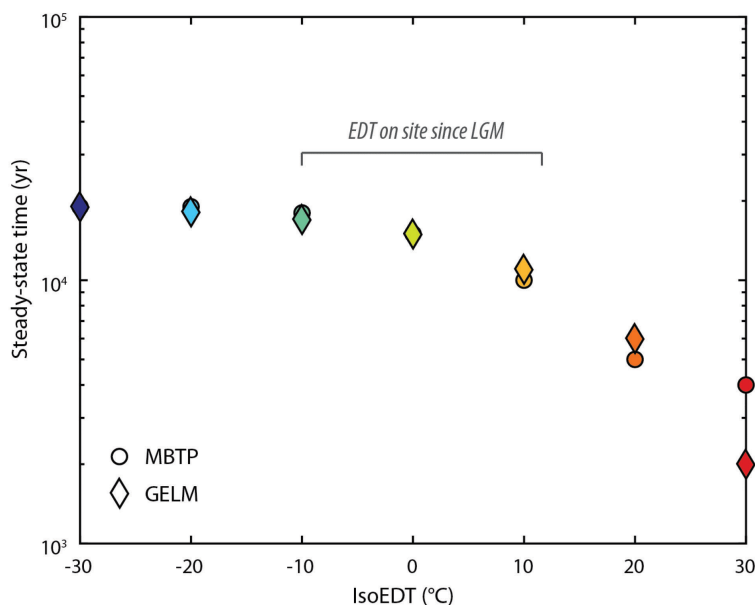
Profile	² Range of Holocene-calibrated parameters				³ Final Holocene-calibrated parameters			⁴ Final laboratory parameters		
	Ea (kJ/mol)	n domain	D_0/a^2 (m^2s^{-1})	Gas fraction (%)	Ea (kJ/mol)	D_0/a^2 (m^2s^{-1})	Gas fraction (%)	Ea (kJ/mol)	D_0/a^2 (m^2s^{-1})	Gas fraction (%)
¹ MBTP	91.5 to 96	d1	11.11 to 12.56	81 to 89	93.5	11.78	85	85.9	9.67	93
		d2	16.11 to 17.77	8 to 10		16.78	9		14.67	6
		d3	8.67 to 10	2 to 9		9.33	6		6.89	1
¹ GELM	96.5 to 100	d1	12.22 to 13.33	47 to 50	98.5	12.89	50	79.5	7.44	43
		d2	16.33 to 17.56	29 to 31		17.11	29		10.33	36
		d3	22.11 to 23.11	21 to 22		22.67	21		16.67	21

¹Diffusion kinetics measurements made on one representative sample per profile: MBTP18-9 (350 μm spherical equivalent radius) and GELM18-1 (450 μm spherical equivalent radius). ²Range of MDD diffusion kinetics parameters obtained by fitting laboratory experimental data and matching ³He concentrations (within 1 σ error) from Holocene calibration samples. ³Best-fitting MDD diffusion kinetics parameters obtained by fitting laboratory experimental data matching ³He concentrations from Holocene calibration samples. ⁴MDD diffusion kinetics parameters based only on laboratory experimental data, and providing the best match in the lower temperature range of the heating schedule (~70-100 °C).

300 In order to explore the theoretical sensitivity (and potential variability) of the MBTP and GELM quartz, we numerically evaluated the time required for the concentration of ³He in each sample to reach steady-state (i.e., thermal loss balanced with cosmic-ray induced production gain) as function of constant EDT. Forward simulations using the ³He diffusion predictive model of Tremblay et al. (2014a, b) and the final Holocene-calibrated diffusion kinetic parameters were thus run for a range of isotherms representative of Earth surface EDTs (hereafter referred to as isoEDTs; tested range from -30 to 30°C), assuming

305 a μm radii and no initial ³He concentration. Equilibrium conditions were assumed to be reached once no significant change in ³He concentration was recorded (<1% per kyr). While we observe some variability in ³He diffusion behavior and derived diffusion kinetics parameters between MBTP and GELM quartz (Fig. 3, Table 2), results from sensitivity tests in terms of steady-state times are relatively similar. For isoEDTs between -10 and 10°C, bracketing approximately potential D_0/a^2 values experienced along both deglaciation profiles between the LGM and today, the time predicted for ³He diffusion to reach

310 equilibrium varies between ~10 kyr (isoEDT of 10°C) and ~20 kyr (isoEDT of -10°C; Fig. 4). Interestingly, while steady-state time estimates remain relatively constant for quartz from both sites at ca. 20 kyr for colder isoEDTs (-10 to -30°C), we observe a pronounced non-linear dependence for EDTs above 0°C, resulting in much shorter equilibrium times in the high EDTs range (less than 5 kyr for EDT above 20 °C, Fig. 4).



315 **Figure 4: Theoretical ^3He steady-state time estimates for isoEDTs varying between -30 to 30 °C, using the final Holocene-calibrated diffusion kinetics parameters determined for each study site, and assuming $450\ \mu\text{m}$ grain radius.**

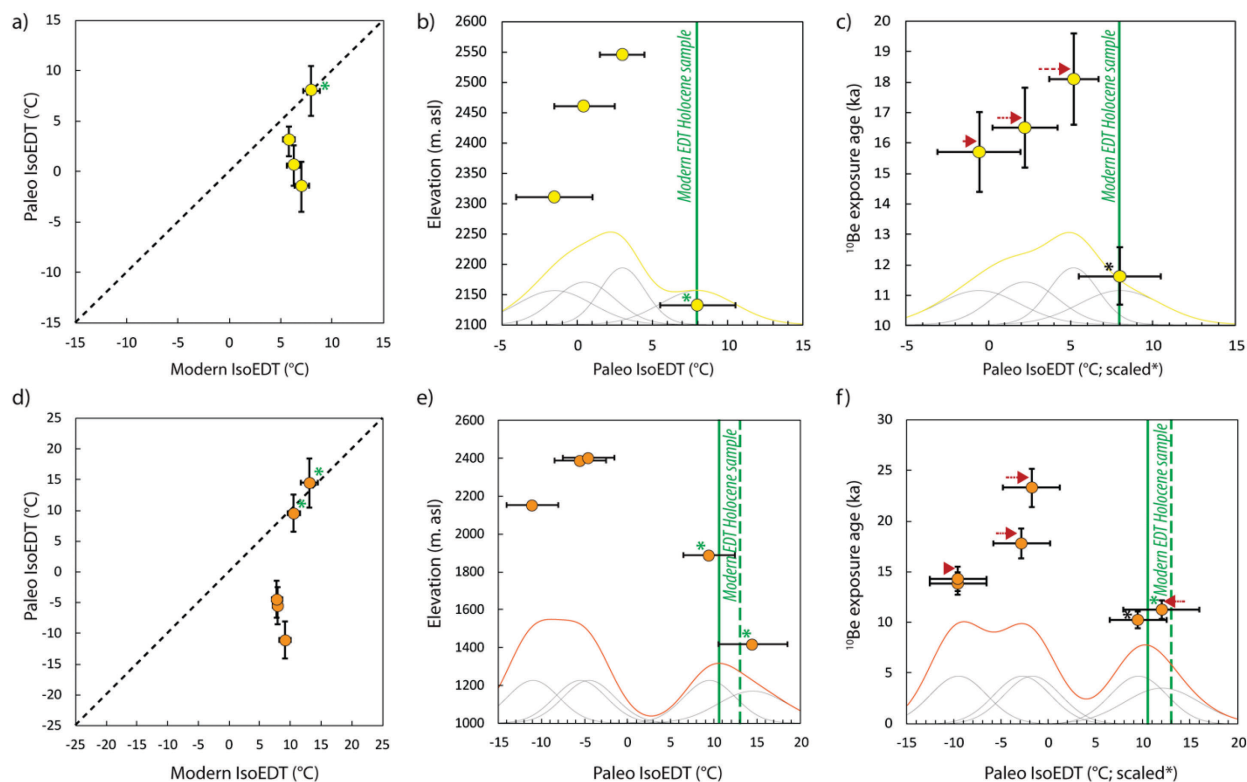
4.2 ^3He exposure ages and PaleoIsoEDTs

For each site, apparent ^3He exposure ages are systematically lower (from 20 to 75%) than apparent ^{10}Be exposure ages (Table 1, Fig. 2). While ^{10}Be ages show a general decrease with elevation, in agreement with progressive ice thinning along a deglaciation profile in the high Alps during the Late Glacial, this trend is less evident for apparent ^3He ages (Fig. 2). The evolution of retention ($^3\text{He}/^{10}\text{Be}$ exposure ages ratio) with elevation differs between the two sites, with an apparent decrease in retention for low-elevation/younger samples along the GELM profile (~ 1500 to 2500 m a.s.l.), which is not visible along the MBTP profile (similar retention between MBTP samples), which is more restricted in elevation range (~ 2100 to 2600 m a.s.l.; Fig. 2).

325 To determine the apparent constant EDT (that we refer to as paleoIsoEDT) from the natural ^3He signal recorded in each sample, ^3He diffusion predictive models (implemented with the final Holocene-calibrated diffusion kinetics) were run for a time period equal to the sample's ^{10}Be exposure age and for a range of isoEDT (isothermal holding between -10 to 15 °C for MBTP; -25 to 20 °C for GELM, 1 °C increment). The isoEDT leading to best-matching synthetic ^3He concentration with the observed natural ^3He concentration was retained as the paleoIsoEDT (Fig. 5, Table 1). As Holocene samples were used to calibrate the diffusion kinetics (cf. Sect. 4.1), it is expected that ^3He derived paleoIsoEDTs from these samples are equivalent to their respective modern EDTs. On the other hand, all pre-Holocene samples at both sites have paleoIsoEDTs that are lower than their corresponding modern EDTs (Fig. 5a, d; Table 1). For the MBTP profile, the difference between modern EDTs and



paleoIsoEDTs varies from around 3 to 9°C. This difference is even greater for the GELM profile, where paleoIsoEDTs are around 12 to 20°C lower than their associated modern EDTs. Pre-Holocene samples are located well above (200 to 500 meters) Holocene samples, and all above 2000 m a.s.l. While paleoIsoEDTs derived from the high-elevation/pre-Holocene samples agree within error for each site, they clearly depart from EDTs obtained from the low-elevation/Holocene sample(s), by ~6° (MBTP site) and ~18°C (GELM site) based on the obtained bimodal distributions (Fig. 5b, e). After correcting for temperature decrease with elevation (assuming a lapse rate of 5°C/km), the difference between pre- and Holocene samples paleoIsoEDTs is still significant for GELM (~10 to 20°C, Fig. 5f). For MBTP, although elevation-corrected paleoIsoEDTs from two high-elevation/pre-Holocene samples (MBTP18-2 and -11) are still clearly distinguishable from the low-elevation/Holocene sample (MBTP18-9; Fig. 5c), the probability distribution appears closer to unimodal since the paleoIsoEDT from the highest sample (MBTP18-1) partially overlap with MBTP18-9.



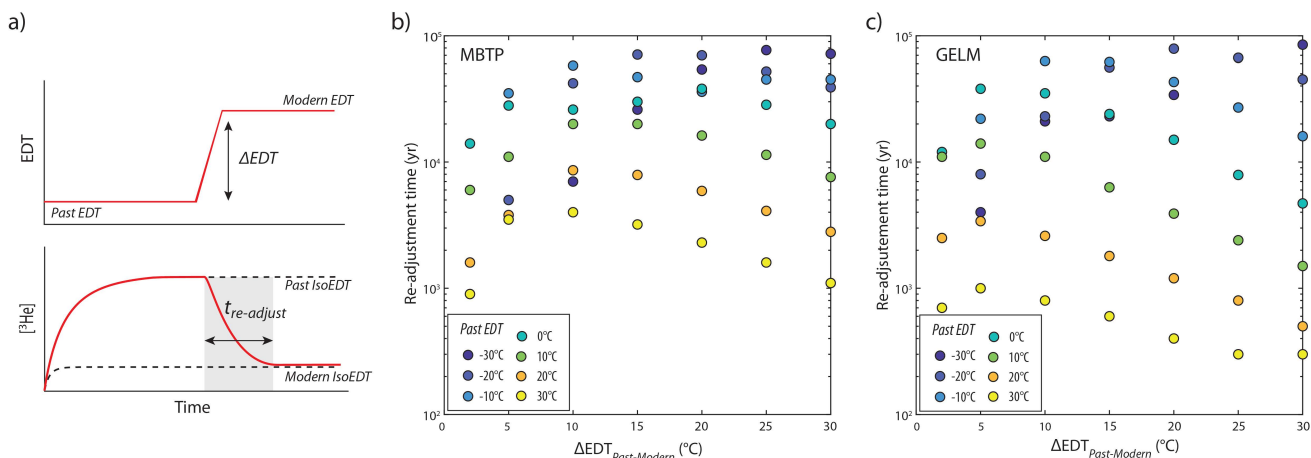
345 **Figure 5: Distribution of ^3He derived paleoIsoEDTs along the MBTP (a-c, top) and GELM (d-f, bottom) deglaciation profiles. Holocene samples used for calibration are marked with an asterisk. (a,d) Paleo-IsoEDTs relative to modern EDTs (black dashed line is 1:1); (b,e) relationship between paleoIsoEDT and elevation, and (c,f) relationship between paleoIsoEDT and ^{10}Be exposure age, after correction for lapse rate (marked by red arrows, relatively to Holocene sample marked with a black asterisk). Green (dashed) lines are modern EDTs for Holocene samples. The thin lines represent the (yellow/orange) of the individual () probability distribution of paleoIsoEDTs.**



350 4.3 Forward simulations with time-varying EDT

Based on global and regional paleoenvironmental records, we can expect that pre-Holocene samples collected at MBTP and GELM sites have experienced at least one main significant temperature change, marking the transition from (colder) Late Glacial to warmer and more stable Holocene conditions (cf. Sect. 1 for details).

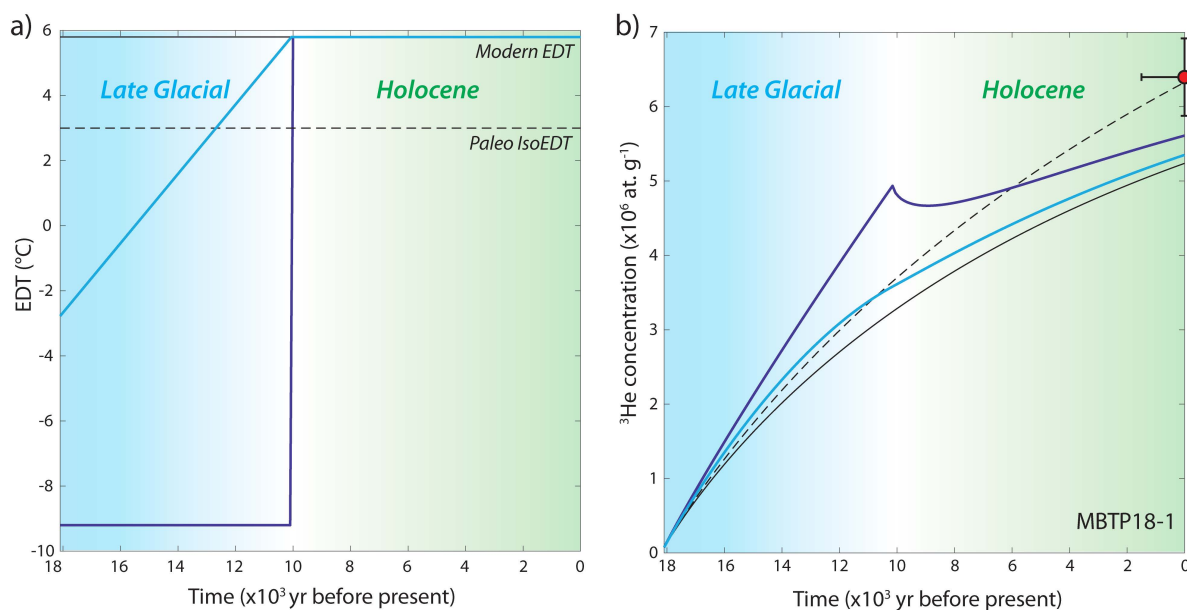
Following this observation, we first investigate the theoretical time needed for the MBTP and GELM ^3He quartz systems to re-adjust to a change in temperature in a warming scenario, assuming that these systems were already at steady-state conditions. Forward simulations (450 μm radii assumed) were run for different time-EDT scenarios involving an initial EDT (ranging from -30 to 30 $^{\circ}\text{C}$; initial ^3He concentration at steady-state with initial EDT) followed by a step warming event (+2, +5, +10, +15, +20, +25, +30 $^{\circ}\text{C}$; over 0.1 to 1 kyr depending on the sensitivity of the quartz system for the considered EDT scenario), after which the resulting warmer EDT was maintained until full re-adjustment of the ^3He -quartz system. We considered full re-adjustment to have occurred when modelled ^3He concentrations following the step warming event reached within 10% the ^3He concentrations expected for an isoEDT equivalent to the final (warmer) EDT (Fig. 6a). We present simulation results in Figures 6b-c. For past EDTs $<0^{\circ}\text{C}$ followed by a step warming up to 20 $^{\circ}\text{C}$, readjustment times are all longer than 10 kyr, either considering MBTP or GELM diffusion kinetics. Estimates of LGM-temperature anomalies suggested for the European Alps are equivalent to an apparent warming of 5 to 15 $^{\circ}\text{C}$ (cf. Sect. 1). When considering EDT scenarios with a similar warming range applied to our study sites with modern EDTs around 5 to 10 $^{\circ}\text{C}$ (at pre-Holocene sampling sites; i.e., equivalent to initial past EDT between 0 to 5 $^{\circ}\text{C}$ and -10 to -5 $^{\circ}\text{C}$ for 5 and 15 $^{\circ}\text{C}$ warming step, respectively), our simulation outcomes show relatively long re-adjustment times from around 20 to 45 kyr (Fig. 6). We should note, however, that these times are maximum estimates since we considered ^3He quartz systems at steady-state conditions with initial cold EDTs before the warming event.



370 **Figure 6: Conceptual approach (a) and output results for MBTP (b) and GELM (c) of ^3He re-adjustment time ($t_{\text{re-adjust}}$) for one-step EDT change scenarios (temperature warming from 2 to 30 $^{\circ}\text{C}$), using the final diffusion kinetics parameters determined for each study site, and assuming 450 μm grain radius. Calculations assume that ^3He concentrations were already at steady-state for past EDT conditions (i.e., as would be expected for infinite exposure time) prior to imposing the temperature change.**



In a second set of experiments, we explore the thermal memory of ^3He in quartz for a step warming EDT scenario fixed in
375 time that is more representative of the post-LGM paleoclimate history in the Alps, including: (1) an initial cold period starting
at 24 ka with an imposed EDT set 15°C lower compared to modern EDT (maximum LGM temperature anomalies, cf. Sect.
1); (2) a warming step to modern EDT that is either progressive from 24 to 10 ka (i.e., consistent with a Younger Dryas-
Holocene transition) or abrupt between 11 and 10 ka, and (3) stable conditions at the modern EDT throughout the Holocene
380 following this scenario, with the time period and the time-dependent EDT variable set accordingly to each sample ^{10}Be
exposure age and modern EDT, respectively. For all GELM and MBTP samples, these forward simulations result in synthetic
 ^3He concentrations significantly lower than their respective measured ^3He concentrations. In Figure 7b we present the results
for sample MBTP18-1, for which we observed the smallest difference between modern EDT and paleoIsoEDT (Fig. 5a; Table
1).



385

Figure 7: a) Simplified warming EDT scenario since the LGM (~24 ka), with progressive and abrupt EDT changes in light and dark blue lines, respectively; b) Synthetic evolution of ^3He concentration (blue lines) compared with the natural ^3He concentration recorded in MBTP18-1 (red circle). The ^3He concentration evolution is also indicated for a constant-temperature scenario at the modern EDT and paleoIsoEDT (set in Figure 5; black solid and dashed lines, respectively). We were unable to reproduce the observed natural ^3He concentration for any samples with pre-Holocene exposure under this simplified LGM EDT scenario.
390

To further investigate potential effects of a larger EDT difference between modern and past conditions, and/or a more recent EDT change, we performed an additional set of simulations using step warming EDT scenarios with more free parameters. Scenarios with an EDT change occurring from 10^4 to 10^2 years ago and with difference between past and modern EDTs (ΔEDT) up to 40°C were tested iteratively on each pre-Holocene sample, assuming no initial ^3He concentration and with total
395 exposure time and EDT variables adjusted accordingly, as described above. Scenarios for which we could reproduce the

observed natural ^3He concentration (within uncertainties) were accepted, resulting in a range of different possible scenarios with varying ΔEDT and time of EDT change for each pre-Holocene sample (Fig. 8). For both sites, we observed a similar pattern between ΔEDT and time of EDT change: the further back in time the EDT change occurs, the greater the ΔEDT that is needed to reproduce observed natural ^3He concentrations. In addition, for any given time of EDT change, ΔEDT s tend to be inversely correlated with sample elevation/ ^{10}Be exposure age. Within these similarities, the two sites differ by the magnitude of the ΔEDT required to reproduce observed natural ^3He concentrations. For example, along the MBTP site (Fig. 8a), ΔEDT s of 5 °C occurring a few kyr ago are required to explain ^3He concentrations measured in the highest/oldest sample (MBTP18-1), while ΔEDT s of 35 °C occurring a few kyr ago are required to explain ^3He concentrations measured from the lowest/youngest pre-Holocene sample (MBTP18-11). For the same sites, ΔEDT s of 3 and 15 °C are required if the EDT change occurred within the last centuries. On the other hand, for the GELM site, our simulations found no ΔEDT solution if the EDT change is applied prior to 1 ka (within our ΔEDT limit of 40 °C; except for GELM18-12; Fig. 8b). In the case of EDT change occurring within the last centuries, ΔEDT s for the GELM samples are significantly larger than for MBTP samples, with ΔEDT s between 15–30 °C required for the highest/oldest samples (GELM18-12 and -1). For the intermediate samples (GELM18-11 and -5) which are also exhibiting the greatest ^3He - ^{10}Be age differences, numerical solutions could only be recovered for very recent EDT changes (≤ 200 yr) and with $\Delta\text{EDT} > 35$ °C.

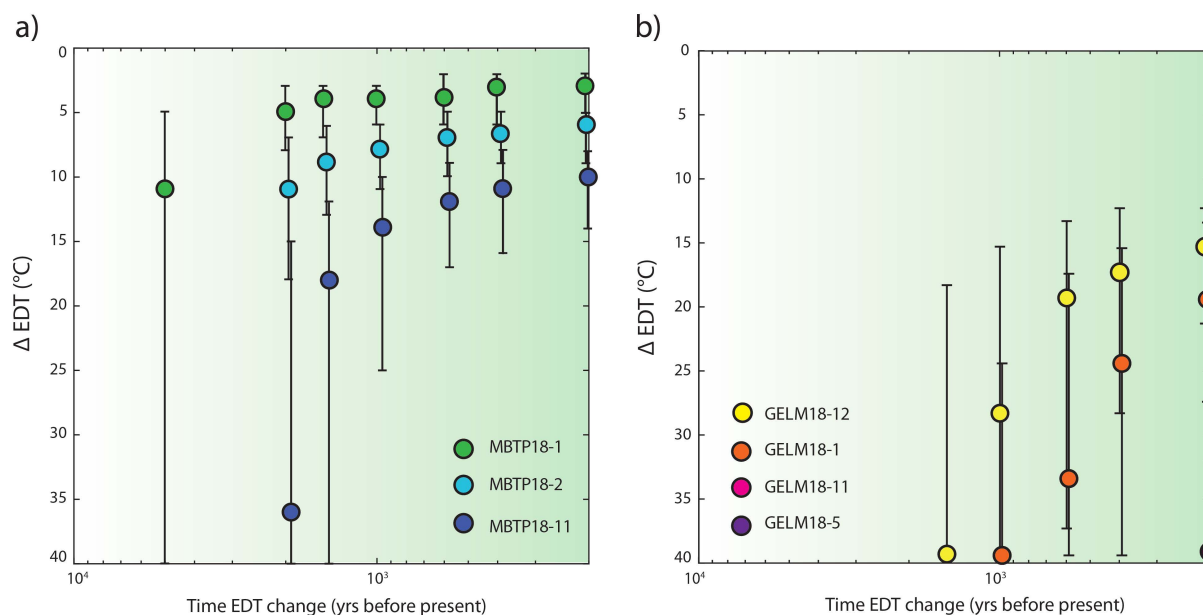


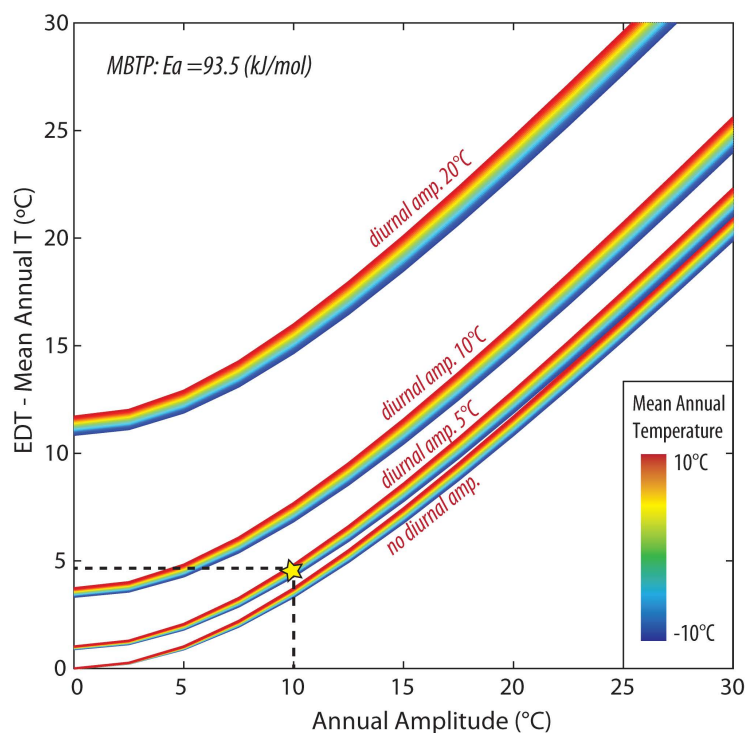
Figure 8: One-step EDT change scenarios that reproduce the observed natural ^3He concentration for each pre-Holocene MBTP (a) and GELM (b) samples, with ΔEDT solution as function of the time of EDT change. The error bars indicate all the possible ΔEDT solutions and the colored circles indicate the best-matching scenario.



415 5 Discussion

5.1 Paleo-environmental ^3He signal interpretation

All studied samples indicate the preservation of a ^3He concentration consistent with temperatures that are colder than present-day EDT conditions at both the MBTP and the GELM sites (paleoIsoEDTs $\sim 3\text{-}9^\circ\text{C}$ and $\sim 12\text{-}20^\circ\text{C}$ lower than modern EDTs, respectively, Fig. 5). However, for both sites, the recorded ^3He concentrations are apparently not concordant with simple time-
420 EDT scenarios describing a plausible post-LGM mean temperature evolution in the European Alps (i.e., LGM mean temperature anomaly up to 15°C , Fig. 7). Even when allowing for a larger EDT difference between LGM and present-day (up to 40°C), modeled ^3He concentrations remain significantly below the observed values at both sites. Such large EDT differences would furthermore not be supported by any mean temperature reconstructions for the European Alps since the LGM (e.g., Heiri et al., 2014a). Likewise, potential variation in seasonal temperature cannot contribute significantly to a larger pre-
425 Holocene EDT anomaly. Indeed, global and regional paleoclimate studies rather suggest a larger seasonal temperature amplitude occurred before the Holocene (e.g., Davis et al., 2003; Buizert et al., 2018), which would have the effect of increasing the paleoEDTs instead (Fig. 9).



430 **Figure 9: Difference between EDT and mean annual temperature as a function of increasing seasonal temperature amplitude for different diurnal temperature amplitudes and assuming an E_a of 93.5 kJ/mol (MBTP site, Holocene-calibrated diffusion kinetics). The yellow star indicates the conditions used to estimate the modern EDT at the sampling sites. Decreasing the annual/diurnal amplitude can yield to up to a $\sim 5^\circ\text{C}$ decrease in the modern EDT. Similar results are obtained when using $E_a = 98.5\text{ kJ/mol}$ (GELM site, Holocene-calibrated diffusion kinetics).**



We attribute the results of modeled ^3He concentrations remaining significantly below the observed ones, despite significant
435 lowering of temperature prior to the Holocene (e.g., Fig. 7), to the damping effect of the Holocene period (the last ~10 kyr),
which is characterized by relatively stable mean temperature conditions similar to present-day. This hypothesis first appears
to contradict our theoretical tests which indicate that the thermal signal inherited from past EDTs 10 to 15°C colder than today
should *a priori* be (partly) preserved for 30-45 kyr under modern EDT conditions (Fig. 6). However, this time range relies on
the assumption that bedrock surfaces were exposed for long enough to past colder conditions before the temperature change
440 occurred, in order to reach ^3He steady-state concentrations (i.e., estimated exposure time around 20 kyr; Fig. 4). Along the
MBTP and GELM profiles, bedrock surfaces have not been exposed for more than 5-8 kyr (MBTP) and 4-13 kyr (GELM)
before the Late Glacial-Holocene transition, resulting in ^3He accumulation up to 35-55% (MBTP) and 30-85% (GELM) of
 ^3He steady-state concentrations when considering paleoIsoEDTs 10-15°C lower than present-day EDTs. In some cases, ^3He re-
adjustment time estimates to modern EDTs are predicted to be reduced by ~90 to 80% for MBTP site and by >90 to 60% for
445 GELM site, implying we should recover the dominance of Holocene temperature conditions in the ^3He signal from the sampled
bedrock surfaces.

Our observed ^3He concentrations can be reproduced by forward simulations with an EDT change occurring on much more recent
time scales (Fig. 8). For the MBTP site, a ΔEDT of 7 to 5°C within the last few thousand years to centuries predicts the
observed natural ^3He concentrations for two pre-Holocene samples (MBTP18-1 and 2; a ΔEDT of 12 to 8°C is required for
450 MBTP18-11). Such a ΔEDT estimate, considering mean temperature fluctuations up to 2°C for the Holocene period (Davis et
al., 2003), would also require variations in diurnal/annual temperature amplitudes to account for an additional 5°C ΔEDT .
However, this would imply the lowering of both diurnal and annual temperature amplitudes to null before modern conditions
(Fig. 9), which contradicts global and regional records that indicate an increased seasonality (and thus larger ΔEDT) in the
early Holocene (Davis et al., 2003; Buizert et al., 2018) compared to the present-day. Furthermore, the forward simulations
455 discussed here (Fig. 8) used diffusion kinetics calibrated on Holocene samples. Therefore, allowing a significant EDT change
over the last 10^2 - 10^3 years is in contradiction with our calibration approach (cf. Sect. 3). If instead we use diffusion kinetics
solely derived from laboratory experiments without Holocene calibration (Fig. 3, Table 2), an even larger recent ΔEDT is
required to explain observed MBTP ^3He concentrations (15 to 25°C or more than 30°C for changes over 10^2 or 10^3 yr,
respectively, Fig. S2b). Such large ΔEDTs are significantly greater than expected EDT variations from changes in mean annual
460 temperatures and/or in annual/diurnal temperature amplitudes during the Holocene. Even greater ΔEDTs are needed to explain
the observed GELM ^3He concentrations using either diffusion kinetics approach: from 15 to more than 35°C (explaining
GELM18-1 and 12 only, for EDT change over 10^2 or 10^3 yr, respectively) when using Holocene-calibrated diffusion kinetics
(Fig. 8b), and to more than 40°C when using laboratory diffusion kinetics (no convergence found within the 40°C ΔEDT limit
for pre-Holocene samples; Fig. S3b), which are in both cases clearly incompatible with plausible Holocene paleoclimatic
465 histories.

Finally, additional potential uncertainties in modern EDT estimates, used to define the EDT of the recent and stable period in the
step warming EDT scenarios (Sect. 4.3), cannot be ruled out. In particular, it is not known to what extent present-day conditions



(based on decadal direct air and ground temperature measurements; cf. Sect. 3.1) are representative over centennial to millennial time scales. Correcting for overestimated diurnal/annual temperature amplitudes and/or mean annual temperatures would result in lower modern (i.e., recent) EDTs (Fig. 9). Assuming an overestimate of 50% in modern diurnal and annual temperature amplitudes, and up to 2°C overestimate in MARST based on recorded mean temperature fluctuations (Davis et al., 2003; Ghadiri et al., 2018, 2020) and applied corrections to MAAT (cf. Sect. 3.1), would lead to ~3.5°C lowering of modern EDTs for MBTP/GELM sites. Applying such an estimated correction to the recent period EDT potentially permits us to resolve observed ³He concentrations for two of the MBTP samples (MBTP18-1 and -2) with ΔEDT of 5 to 10°C for a change occurring at ca. 10 ka (i.e., LGM scenario; Fig. S2c). It is also worth noting that natural ³He MBTP concentrations for those samples can be reproduced with minor ΔEDTs (≤1.5°C) over recent timescales (10²-10³ yr). When using laboratory-derived diffusion kinetics without Holocene calibration, *a priori* more appropriate to explore recent EDT changes, only scenarios with more than -10°C ΔEDT within the last thousand years are accepted (Fig. S2d), inconsistent with paleoclimatic records over this recent time period. For GELM samples, correcting modern/recent EDT does not permit to reproduce the observed ³He concentrations with plausible ΔEDTs for EDT change occurring at the Late Glacial-Holocene transition (ca. 10 ka; no solution), nor on more recent timescales (Fig. S3c-d).

5.2 Potential geological uncertainties

Several sources of geological uncertainties may affect the results obtained in this study. At first, our approach relies on the assumption that bedrock surfaces have experienced a simple exposure history along the time period recorded by ¹⁰Be concentrations, without pre-exposure or episodic coverage. Depth profiles of ¹⁰Be measurements on glacially-polished bedrocks in the western Alps, with apparent exposure ages of 10-20 ka, indicate that an inherited ¹⁰Be concentration due to insufficient glacial erosion may persist and could lead to up to 9% age overestimates (Prud'Homme et al., 2020). Similarly, Wirsig et al. (2016b) suggested potential but limited pre-LGM (less than a few ka overestimate) inheritance for some GELM samples. While previous bedrock surface exposure would also imply an inherited ³He concentration, the latter would be subject to diffusion (partial or total) during glacier coverage (contrary to ¹⁰Be which would experience only minor radioactive decay over 10-100 ka timescales). Considering such a scenario (i.e., inheritance/complex exposure history) would hence result in lower ³He concentrations recorded by bedrock surfaces regardless of the temperature history experienced by the rock surface during the total ¹⁰Be exposure period (i.e., lower ³He/¹⁰Be ratio; Balco et al., 2016). This scenario is also valid for post-LGM episodic coverage. Such effects are however expected to be minor considering the limited potential ¹⁰Be inheritance (<10%) from pre-LGM exposure, as well as the unlikelihood of prolonged coverage of the relatively steep (i.e., no loose sediments/thick snow accumulation) and high (i.e., above tree line) sampled bedrock surfaces. Moreover, attempting to correct for these processes would result in opposite effects than what we observed for MBTP and GELM samples, with even lower paleoIsoEDT estimates and greater ΔEDTs required for warming EDT scenarios to recover observed natural ³He concentrations.



500 An additional source of uncertainty is postglacial erosion of sampled bedrock surfaces, assumed to be negligible in this study. Based on a combined approach exploiting cosmogenic ^{10}Be and Optically Stimulated Luminescence (OSL) systems, Lehmann et al. (2020) suggested potential high postglacial erosion rates (above 3.5 mm/kyr) for low-elevation MBTP samples. Other regional estimates for crystalline bedrock commonly indicate Alpine postglacial erosion rates of 0.1 to 1 mm/kyr (Kelly et al., 2006; Dielforder and Hetzel, 2014; Wirsig et al., 2016b), in line with estimates from other studies (André, 2002; Balco, 2011).

505 Relatively low postglacial erosion rates are further supported along our study sites by the presence of still visible glacial striations (Wirsig et al., 2016b). Applying an erosion correction (0.1 to 1 mm/kyr) will only moderately affect apparent ^{10}Be exposure ages (<1 ka change), and would result in lower predicted ^3He concentrations compared to our observed ones. In summary, geological uncertainties related to exposure history and postglacial surface erosion are generally small and overall do not resolve the significant discrepancy between the natural ^3He signal recorded in pre-Holocene MBTP and GELM samples

510 and modeled ^3He concentrations from expected EDT histories. On the other hand, some of the observed differences may relate to uncertainties regarding the ^3He production rate ($P_{3\text{He}}$) in quartz. Directly estimating $P_{3\text{He}}$ in quartz from geological calibration sites is challenging, as ^3He diffuses from quartz at Earth surface temperatures over 10^2 - 10^4 yr time scale. Alternative approaches using artificial targets (e.g., Vermeesch et al., 2009) or scaling $P_{3\text{He}}$ measured in other retentive minerals (i.e., feldspar; Masarik and Reedy, 1996) have hence been used. While in

515 this study we adopted the Stone (2000)-scaled $P_{3\text{He}}$ from Vermeesch et al. (2009; i.e., $116 \text{ at.g}^{-1}.\text{yr}^{-1}$), a 10% higher ^3He production rate has also been proposed (e.g., Ackert et al., 2011). Applying an increased $P_{3\text{He}}$ (Stone-scaled $P_{3\text{He}} = 128 \text{ at.g}^{-1}.\text{yr}^{-1}$) in general leads to smaller ΔEDTs in order to match the measured ^3He concentrations, as well as an older range of possible times for the EDT change. For MBTP site, however, we could not reproduce ^3He concentrations for an EDT change at 10 ka (except for MBTP18-1; Fig. S2e, Holocene-calibrated diffusion kinetics). Likewise, for more recent changes (10^2 - 10^3

520 yr; laboratory-derived diffusion kinetics without Holocene calibration; Fig. S2f), the resulting ΔEDTs (10 to 25°C) are still not compatible with plausible Holocene temperature conditions. Similar results were obtained for the GELM Late Glacial samples when adopting a 10% increase in $P_{3\text{He}}$ (Fig. S3e, f).

In addition to a higher cosmogenic ^3He production rate, another possibility that we have not accounted for is non-cosmogenic sources of ^3He , specifically nucleogenic ^3He produced by (n, α) reactions with ^6Li . Unaccounted for nucleogenic ^3He would

525 result in lower true cosmogenic ^3He concentrations, which would have the effect of reducing the ΔEDTs at our sample sites toward more realistic values. However, we think it is unlikely that there is significant nucleogenic ^3He in our samples for several reasons. Based on the diffusion kinetics of ^3He in quartz, we anticipate that any nucleogenic ^3He produced in our samples over geologic timescales will be diffusively lost before the quartz is exhumed at near-surface temperatures. Furthermore, the production rate of nucleogenic ^3He is low compared to the cosmogenic production rate of ^3He . We do not

530 have major and trace element data for the MBTP and GELM samples in order to calculate the nucleogenic ^3He production rate directly. However, we can say that a rough maximum estimate for the production rate of nucleogenic ^3He in the GELM samples is $\sim 1 \text{ at/g/yr}$, which is based on a maximum Li concentration of 70 ppm for the Aare granite (Schaltegger and Krähenbühl, 1990) and the production rate estimate of Farley et al. (2006) for an ‘average’ granite. This is 0.3% of the local, scaled



535 production rate of cosmogenic ^3He for sample GELM18-9, which has the lowest cosmogenic ^3He production rate of all of our samples. The combined low retentivity and small production rate of nucleogenic ^3He indicate that this does not contribute significantly to our measured ^3He concentrations, and is therefore unlikely to affect our modeled ΔEDTs in any significant way.

5.3 ^3He diffusion kinetics and ^3He thermal signal

540 Cosmogenic ^3He paleothermometry is still in its early-stage of development for application to Quaternary geology (Tremblay et al., 2014a, b; 2018). At present, there are nontrivial uncertainties related to the interpretation of ^3He diffusion kinetics in quartz, specifically regarding how to extrapolate diffusion kinetics data obtained in laboratory experiments down to Earth surface temperatures in order to interpret natural cosmogenic ^3He concentrations.

545 Noble gas diffusion in minerals is generally assumed to have an Arrhenius-type dependence on temperature, where diffusivity increases exponentially with temperature, and inversely with the diffusion domain size (e.g., Baxter, 2010 and references therein). Interestingly, theoretical studies investigating the fundamentals of ^3He diffusion in quartz predict considerably lower E_a (and much higher diffusivity) than expected when considering a perfect quartz crystal (~20 to 50 kJ/mol; Kalashnikov et al., 2003; Lin et al., 2016; Domingos et al., 2020; Liu et al; 2021), the latter suggesting that no ^3He should be retained over geological timescales at Earth surface temperatures. These results are, however, in contradiction with common observations of ^3He retention in natural rock surfaces (e.g., Brook et al., 1993; Brook and Kurz, 1993; Tremblay et al., 2018) and with
550 typical E_a values empirically determined from laboratory-degassing experiments (between 70 to 100 kJ/mol; Shuster and Farley, 2005; Tremblay et al., 2014b). Furthermore, previous ^3He -degassing experiments conducted on quartz from various origins indicate a large variability in diffusion kinetics (i.e., E_a and D_0) and diffusion behavior, wherein some quartz samples exhibit complex ^3He diffusion behavior while others exhibit a simple, linear Arrhenius dependence (Tremblay et al., 2014b). Both the observed variability and the discrepancy with theoretical predictions suggest that ^3He diffusion in natural quartz is
555 largely governed by sample-specific crystal defects (e.g., structural defects, radiation damages; Domingos et al., 2020), advocating for the use of sample-specific diffusion kinetics (Tremblay et al., 2014b). Complex, non-linear diffusion behavior has been previously observed for argon diffusion in feldspar (e.g., Berger and York, 1981; Harrison and McDougall, 1982) that is analogous to the complex ^3He diffusion behavior observed in some quartz samples. Lovera et al. (1989; 1991) proposed a multi-diffusion domain (MDD) model to account for complex argon diffusion behavior which describes the simultaneous
560 diffusion of discrete, non-interacting intracrystalline sub-domains (e.g., sub-grain fragments) characterized by different effective diffusion lengthscales. Tremblay et al. (2014b) applied the MDD model framework to ^3He diffusion in quartz for samples that exhibited complex Arrhenius behavior, and we have adopted the same approach here.

565 However, it remains an open question as to whether MDD-type models are applicable to quartz ^3He paleothermometry. In Antarctica (Pensacola Mountains), both a single-diffusion domain model using diffusion kinetics from Shuster and Farley (2005) and a two-domain model using kinetics from four local erratics could successfully explain the ^3He signal observed in a series of Holocene samples (Tremblay et al., 2014a; Balco et al., 2016), with a similar predicted ^3He concentration evolution

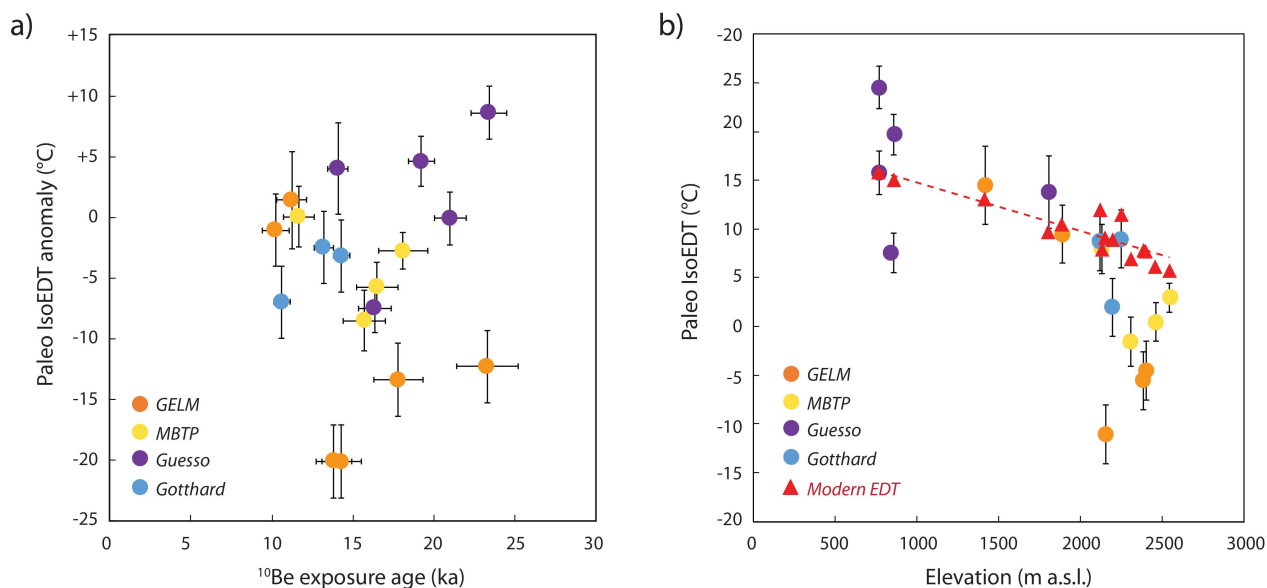


570 between the two approaches over this timescale (Balco et al., 2016). However, each approach could only partially explain the ^3He signal recorded in samples with older ^{10}Be exposure ages, with complex exposure history and/or significant inter-sample variability in diffusion kinetics (e.g., different quartz sources for the sandstone lithology) likely acting as compounding factors (Balco et al., 2016). Additional quartz ^3He analyses using a MDD model and sample-specific diffusion kinetics were recently conducted on moraine boulders from the Gesso Valley in the Italian Alps with LGM to Late Glacial chronologies (Tremblay et al., 2018). PaleoIsoEDTs within the range of their respective modern EDTs were obtained for two out of five samples, with no clear trend between paleoIsoEDTs and boulder (^{10}Be) exposure ages/relative moraine age, in addition to significant intra-moraine variability. Tremblay et al. (2018) highlighted multiple sources of potential uncertainties related to local shading effects (i.e., vegetation, snow cover, topography), grain-size scaling, and complex boulder exposure history, which could have contributed to the observed ^3He signal inconsistencies.

In this study, bedrock-surface samples were purposefully collected along high-elevation valley profiles progressively deglaciated between the LGM and Holocene, with the aim to limit the potential for complex exposure (Sect. 5.2). Diffusion kinetics parameters were measured on one representative sample per profile (MBTP18-9 and GELM18-1). Although inter-sample diffusion kinetics variability cannot be excluded, the apparent homogeneous igneous lithology along each profile supports the representativeness of our chosen sample per profile for diffusion kinetics experiments. Based on this first-order assumption, we noted different ^3He diffusion trends between MBTP and GELM representative samples. MBTP quartz exhibits a nearly simple (i.e., linear; Fig. 3a) Arrhenius diffusion behavior, and measured ^3He concentrations recorded along the MBTP profile can potentially be interpreted as at quasi-equilibrium with respect to modern EDTs (despite a slight trend towards colder signal) when considering the potential sources of uncertainty (e.g., Holocene EDT, $P_{3\text{He}}$ etc., Sect. 5.1 and 5.2; based on the Holocene-calibrated diffusion kinetics). On the contrary, GELM quartz is characterized by complex ^3He diffusion behavior (Fig. 3b), and bedrock surfaces record a ^3He thermal signal that is apparently well colder than their modern EDTs when using diffusion kinetics derived from a MDD framework (calibrated on Holocene samples). This apparent divergence cannot be resolved within the multiple sources of geologic uncertainties, and can be explained by plausible fluctuations in thermal variables (i.e., mean annual temperature and diurnal/annual amplitudes) during the Late Glacial and Holocene time periods. One possible interpretation of these results would be that the MDD model we applied to the GELM samples does not accurately represent ^3He diffusion in quartz that occurred during exposure time. This could be because the MDD model does not adequately represent the physical process of ^3He diffusion in quartz. From a mineralogical perspective, it is indeed unclear if potential processes involved in the formation of sub(-grain) domains (e.g., cooling, alteration, deformation) are consistent with the assumed conditions of the MDD model, i.e., disconnected sub-domains with fixed volumes, Fickian and isotropic diffusion, and zero concentration boundary conditions (e.g., Lovera et al., 1991; Baxter et al., 2010). While MDD models have been successfully applied in a number of thermochronology applications (Reiners et al., 2005 and references therein), deformation processes may also lead to interconnected sub-grain microstructures (e.g., Reddy et al., 1999), in which case the MDD model may be inappropriate for obtaining accurate thermal constraints, as already acknowledged in the literature (e.g., Lovera et al.,



2002; Harrison and Lovera, 2013). On the other hand, alternative diffusion models involving multi-path diffusion (e.g., Lee, 1995) are also suffering from substantial theoretical and experimental gaps (Harrison and Lovera, 2013; Baxter et al., 2010). Alternatively, we cannot rule out that a MDD model for quartz ^3He paleothermometry (Tremblay et al., 2014b) is applicable on both MBTP and GELM quartz, but that the diffusion kinetics and/or the predictive ^3He diffusion model over Earth surface temperatures are inaccurately constrained. The MDD models we implemented do not provide unique solutions to our laboratory-measured diffusion kinetics, which we then extrapolate down to Earth surface temperatures ($<30^\circ\text{C}$). This is illustrated by the significant difference between modern EDTs and estimated paleoIsoEDTs observed for Holocene samples (both MBTP and GELM sites) when using laboratory-derived diffusion kinetics without Holocene calibration (Fig. S4), which therefore supports the additional Holocene calibration step applied in this study. However, our chosen approach still remains relatively crude considering all possible uncertainties related to samples thermal and exposure history (Sect. 5.2 and 5.3). As a consequence, we may consider that the apparently colder signals recorded by ^3He analyses along both profiles (although less pronounced in MBTP) are real, but that these cannot currently be well quantified in terms of surface paleoEDTs. We also compiled all quartz ^3He paleoIsoEDTs available in the European Alps (Tremblay et al., 2018; Guralnik et al., 2018; this study; Fig. 10). Interestingly, while this compilation reveals no apparent relationship with ^{10}Be exposure age (from LGM to Holocene; Fig. 10a), we observe an apparent negative correlation between samples paleoIsoEDT and elevation (Fig. 10b). Furthermore, while samples at low to moderate elevations have paleoIsoEDTs that are relatively consistent with their estimated modern EDTs along an apparent linear lapse rate (around $-0.5^\circ\text{C}/100\text{m}$ lapse rate), paleoIsoEDTs recorded in rock surfaces above $\sim 2200\text{ m a.s.l.}$ clearly depart from modern EDTs/lapse rate trend with significantly "colder" ^3He signals. Although the compiled Alpine dataset is still limited, such an observed distribution raises the question of the influence of rock-surface elevation on ^3He signal records. One hypothesis is that ^3He release from quartz minerals over geological timescales is less effective than predicted by current ^3He diffusion models for the colder temperatures ranges inherent to high-elevation settings. Alternatively, we can suggest that the recorded "colder" ^3He signals in high-elevation samples may reflect recent changes in Alpine permafrost ground conditions. Indeed, bedrock-surface samples above $\sim 2200\text{ m}$ are located close to or in the lower range of sporadic to discontinuous permafrost distribution in the present-day Alps (Magnin et al., 2015; Hoock et al., 2012b). Recent warming after the Little Ice Age is expected to have led to permafrost degradation and restriction of its spatial distribution towards higher elevations (Magnin et al., 2015a, 2017). We hence cannot exclude that those high-elevation bedrock surfaces may have experienced permanent permafrost conditions until recently (i.e., last tens to hundreds of years), where the past MARSTs were thus lower (sub-zero range) than modern MARST estimates scaled on mean annual air temperature (Table 1; Sect. 3.1.). In that case, the recent change in climate conditions over the last decades to centuries would have resulted in both mean annual temperature increases and amplification of annual and diurnal temperature oscillations at the sampling sites greater than those constrained from air temperature records (Etzelmüller et al., 2020) due to the transition from a permafrost to non-permafrost zone. To test these hypotheses (i.e., ^3He diffusion inaccurately constrained at Earth surface temperature and recent permafrost degradation effects) would require further quartz ^3He measurements at high-elevations and in other Alpine/cold regions.



635 **Figure 10: (a) Relationship between ^3He paleoIsoEDT anomaly and ^{10}Be exposure age from available data from moraine boulders and glacially-scoured bedrock surfaces in the Alps (results from this study, Tremblay et al., 2018 (Guesso) and Guralnik et al., 2018 (Gotthard)). (b) Relationship between ^3He paleoIsoEDT and elevation for same dataset as in (a).**

6 Conclusion

640 Paleoglacier fluctuations in alpine settings lack direct constraints of associated past temperature and/or precipitation conditions, essential to improve our understanding of the response of glaciers and (para)glacial processes to past and future climate forcing changes. In this study, we applied quartz ^3He cosmogenic paleothermometry to derive *in situ* paleo-temperature (EDT) estimates along two deglaciation sequences gradually exposed from the Last Glacial Maximum to the Holocene in the western/northern European Alps (Mont Blanc and Aar massifs, MBTP and GELM respectively). Investigation of quartz ^3He diffusion kinetics indicates a clear difference between the two study sites, with quasi-linear vs. complex diffusion behaviors.

645 Based on the assumption that the same diffusion kinetics parameters apply to all samples at each site, forward numerical simulations of ^3He production and diffusion suggest that no thermal signal from the Late Glacial period should be preserved in investigated rock surfaces with brief exposure durations (several kyr) before the transition to relatively stable Holocene climatic conditions like present-day. However, all our rock-surface samples exposed prior to Holocene indicate an apparent ^3He thermal signal significantly colder than present-day conditions. Our recorded ^3He signals cannot be explained by realistic post-LGM mean annual temperature evolution in the European Alps (as recorded by other paleoclimatic proxies), neither by

650 changes in annual and/or diurnal temperature oscillations at the study sites.

When accounting for potential uncertainties related to Holocene thermal conditions and quartz ^3He production rate, the ^3He signals (ΔEDT) recorded along the MBTP site can potentially be interpreted to be close to equilibrium with present-day/Holocene conditions, with minor change in mean annual temperature or diurnal/annual temperature oscillations. However,



655 ^3He derived paleo-EDTs along the GELM site remain distinctively colder than present-day conditions. One hypothesis is that
the multi-diffusion domain models applied to characterize the observed complex diffusion behavior in the GELM quartz does
not accurately quantify quartz ^3He diffusion in the samples of this site throughout their exposure histories. Alternatively, if the
660 general colder trend recorded along both profiles is possible, the assumed quartz ^3He diffusion kinetics and diffusion models
may inaccurately extrapolate to Earth surface temperatures, precluding quantitative EDT constraints from the observed ^3He
abundances in these samples. Finally, considering the high elevations of the investigated rock-surface samples (> 2000 m), it
is also possible that our ^3He thermal signals result from much more recent changes in Alpine permafrost ground conditions
during the past decades/centuries. While data presented in this study demonstrate the promising use of ^3He cosmogenic
paleothermometry to quantify past environmental changes, additional ^3He analyses in high-alpine/cold settings would be
665 necessary to clarify to which phenomenon the ^3He thermal signal most responsive, i.e., between Late-Pleistocene ambient
temperature variations and recent changes in permafrost distribution.

Code availability

The source codes (with examples of input dataset) used to determine (1) ^3He diffusion kinetics from a step-heating experiment
applying a MDD model framework (example diffusion data from MBTP18-9) and to (2) conduct forward simulation of ^3He
production/diffusion along a given time-EDT scenario (simplified LGM scenario for MBTP18-1 as example, Fig. 7) are
670 available on Zenodo at <https://doi.org/10.5281/zenodo.5808021> (Tremblay, 2021).

Data availability

No additional data are used in this paper that are not supplied in the Supplement.

Supplement link

The supplement related to this article is available online

675 Author contributions

NG and PGV designed the study. NG led fieldwork campaigns, with support of BG, and prepared samples for laboratory
analysis. NG, GB, MMT and DLS conducted the measurements. NG performed the numerical experiments using the model
developed by MMT and GB. NG led the manuscript preparation, with contributions from all co-authors to the analysis and
interpretation of the data, manuscript writing and review.



680 **Competing interests**

Some authors are members of the editorial board of Geochronology. The peer-review process was guided by an independent editor. The authors declare no other conflict of interest.


Acknowledgments

This work was supported by the Swiss National Science Foundation (Grant PP00P2_170559), with measurements at BGC in
685 part supported by the Ann and Gordon Getty Foundation. PGV acknowledges support from the French ANR-PIA program
(ANR-18-MPGA-0006). MMT acknowledges support from the U.S. National Science Foundation (OPP-1935945) and the
AAAS Marion Milligan Mason Fund. We thank Benjamin and Fred Lehmann, and Guilhem A. Douillet for their help in the
field to collect samples.

References

690 Abrecht, J.: Geologic units of the Aar massif and their pre-Alpine rock associations: a critical review, *Schweizerische
Mineralogische und Petrographische Mitteilungen*, 74, 5–27, 1994.

Ackert, R.P., Mukhopadhyay, S., Pollard, D., DeConto, R.M., Putnam, A.E., and Borns, H.W.: West Antarctic Ice Sheet
elevations in the Ohio Range: Geologic constraints and ice sheet modeling prior to the last highstand. *Earth and Planetary Sc.*
695 *Lett.*, 307, 1-2, 83–93, doi:10.1016/j.epsl.2011.04.015, 2011.

Affolter, S., Häuselmann,  Fleitmann, D., Lawrence Edwards, R., Cheng, H., and Leuenberger, M.: Central Europe
temperature constrained by speleothem fluid inclusion water isotopes over the past 14,000 years, *Science Advances*, 5,
eaav3809, doi:10.1126/sciadv.aav3809, 2019.

700

Allen, R, Siegert, M.J., and Payne, A: Reconstructing glacier-based climates of LGM Europe and Russia – Part 2: A dataset
of LGM precipitation/temperature relations derived from degree-day modelling of palaeo glaciers, *Clim. Past*, 4, 249–263,
doi:10.5194/cp-4-249-2008, 2008.

705 André, M-F.: Rates of postglacial rock weathering on glacially scoured outcrops (Abisko-Riksgränsen area, 68°N), *Geogr.
Ann.*, 84, 139–150, doi:10.1111/j.0435-3676.2002.00168.x, 2002.

Balco, G.: Contributions and unrealized potential contributions of cosmogenic-nuclide exposure dating to glacier chronology,
1990-2010. *Quaternary Sci. Rev.*, 30, 3–27, doi:10.1016/j.quascirev.2010.11.003, 2011.



710

Balco, G., Stone, J.O., Lifton, N.A., and Dunai, T.J.: A complete and easily accessible means of calculating surface exposure ages or erosion rates from ^{10}Be and ^{26}Al measurements, *Quat. Geochronol.*, 3, 174–195, doi: 10.1016/j.quageo.2007.12.001, 2008.

715

Balco, G., Todd, C., Huybers, K., Campbell, S., Vermeulen, M., Hegland, M., Goehring, B.M., and Hillebrand, T.: Cosmogenic-nuclide exposure ages from the Pensacola Mountains adjacent to the foundation ice stream, Antarctica, *Am. J. Sci.*, 316, 542–577, doi:10.2475/06.2016.02, 2016.

720

Baroni, C., Gennaro, S., Cristina, M., Ivancich, S., Christl, M., Cerrato, R., and Orombelli, G.: Last Lateglacial glacier advance in the Gran Paradiso Group reveals relatively drier climatic conditions established in the Western Alps since at least the Younger Dryas, *Quaternary Sci. Rev.*, 255, 106815, doi:10.1016/j.quascirev.2021.106815, 2021.

725

Bartlein, P.J., Harrison, S.P., Brewer, S., Connor, S., Davis, B.A.S., Gajewski, K., Guiot, J., Harrison-Prentice, T.I., Henderson, A., Peyron, O., Prentice, I.C., Conzatti, M., Seppä, H., Shuman, B., Sugita, S., Thompson, R.S., Viau, E.A., Williams, J., and Wu, H.: Pollen-based continental climate reconstructions at 6 and 21 ka: a global synthesis, *Clim. Dynam.* 37, 775–802. doi:10.1007/s00382-010-0904-1, 2010.

Baxter, E.F.: Diffusion of noble gases in minerals, *Rev. Mineral. Geochem.*, 72, 509–557, doi: 10.2138/rmg.2010.72.11, 2010.

730

Becker, P., Seguinot, J., Juvet, G., and Funk, M.: Last Glacial Maximum precipitation pattern in the Alps inferred from glacier modelling, *Geographica Helvetica* 71, 173–187, <https://doi.org/10.5194/gh-71-173-2016>, 2016.

Berger, G. W., York, D., and Dunlop, D. J.: Calibration of Grenvillian palaeopoles by $^{40}\text{Ar}/^{39}\text{Ar}$ dating, *Nature* 277, 46–48, doi:10.1038/277046a0, 1979.

735

Beyerle, U., Purtschert, R., Aeschbach-Hertig, W., Imboden, D.M., Loosli, H.H., Wieler, R., and Kipfer, R.: Climate and Groundwater Recharge During the Last Glaciation in an Ice Covered Region, *Science* 282, 731–734, doi: 10.1126/science.282.5389.731, 1998.

740

Boeckli L., Brenning A., Gruber S., and Noetzi J.: A statistical approach to modelling permafrost distribution in the European Alps or similar mountain ranges, *The Cryosphere*, 6, 125–140, doi:10.5194/tc-6-125-2012, 2012a.



- Boeckli, L., Brenning, A., Gruber, S., and Noetzli, J.: Permafrost distribution in the European Alps: calculation and evaluation of an index map and summary statistics, *The Cryosphere*, 6, 807–820, doi:10.5194/tc-6-807-2012, 2012b.
- 745
- Borchers, B., Marrero, S.M., Balco, G., Caffee, M., Goehring, B., Lifton, N., Nishiizumi, K., Phillips, F.M., Schaefer, J., and Stone, J.O.: Geological calibration of spallation production rates in the CRONUS-Earth project, *Quat. Geochronol.*, 31, 188–198, doi:10.1016/j.quageo.2015.01.009, 2015.
- 750
- Brook, E.J., and Kurz, M.D.: Surface-exposure chronology using in situ cosmogenic ^3He in antarctic quartz sandstone boulders, *Quaternary Res.*, 39, 1–10, doi:10.1017/S0954102008001478, 1993.
- Brook, E.J., Kurz, M.D., Ackert Jr., R.P., Denton, G.H., Brown, E.T., Raisbeck, G.M., and Yiou, F.: Chronology of glacier advances in Arena Valley, Antarctica, using in situ cosmogenic ^3He and ^{10}Be , *Quaternary Res.*, 39, 11–23, doi:10.1006/qres.1993.1002, 1993.
- 755
- Luizert, C., Keisling, B. A., Box, J. E., He, F., Carlson, A. E., Sinclair, G., and DeConto, R. M.: Greenland-wide seasonal temperatures during the last deglaciation, *Geophys. Res. Lett.* 45, 1905–1914, doi:10.1002/2017GL075601, 2018.
- Christodoulides, C., Ettinger, K.V., and Fremlin, J.H.: The use of TL glow peaks at equilibrium in the examination of the thermal and radiation history of materials, *Mod. Geol.* 2, 275–280, 1971.
- 760
- Clark, P.U., Dyke, A.S., Shakun, J.D., Carlson, A.E., Clark, J., Wohlfarth, B., Mitrovica, J.X., Hostetler, S.W. and McCabe, A.M.: The Last Glacial Maximum, *Science*, 325, 710–714, doi:10.1126/science.1172873, 2009.
- 765
- Clark, P.U., Shakun, J.D., Baker P.A., Bartlein, P.J., Brewer, S., Brook, E., Carlson, A.E., Cheng, H., Kaufman, D.S., Liu, Z., Marchitto, T.M., Mix, A.C., Morrill, C., Otto-Bliesner, B.L., Pahnk, K., Russell, J.M., Whitlock, C., Adkins, J.F., Blois, J.L., Clark, J., Colman, S.M., Curry, W.B., Flower, B.P., He, F., Johnson, T.C., Lynch-Stieglitz, J., Markgraf, V., McManus, J., Mitrovica, J.X., Moreno, P.I., and Williams, J.W.: Global climate evolution during the last deglaciation, *P. Natl. Acad. Sci. USA*, May 109, 19, E1134–E1142, doi:10.1073/pnas.1116619109, 2012.
- 770
- Cook, S.J., Swift, D.A., Kirkbride, M.P., Knight, P.G., and Waller, R.I.: The empirical basis for modelling glacial erosion rates, *Nat. Commun.*, 11, 759, doi:10.1038/s41467-020-14583-8, 2020.
- Davis, B.A.S., Brewer, S., Stevenson, A.C., Guiot, J., and Data contributors: The temperature of Europe during the Holocene reconstructed from pollen data, *Quaternary Sci. Rev.*, 22, 1701–1716, doi:10.1016/S0277-3791(03)00173-2, 2003.
- 775

Dielforder, A., and Hetzel, R.: The deglaciation history of the Simplon region (southern Swiss Alps) constrained by ^{10}Be exposure dating of ice-molded bedrock surfaces. *Quaternary Sci. Rev.*, 84, 26–38, doi:10.1016/j.quascirev.2013.11.008, 2014.

780 Dobmeier, C.: Variscan P–T deformation paths from the southwestern Aiguilles Rouges massif (External massif, western Alps) and their implication for its tectonic evolution, *Geol. Rundsch.* 87, 107–123, doi:10.1007/s005310050193, 1998.

Domingos, R, Tremblay, M.M., Shuster, D.L., and Militzer, B.: Simulations and Experiments Reveal Effect of Nanopores on Helium Diffusion in Quartz, *ACS Earth Space Chem.*, 4, 1906–1912, doi:10.1021/acsearthspacechem.0c00187, 2020.

785

Ehlers, J., Gibbard, P.L., and Hughes, P.D., (Eds.): *Quaternary Glaciations - Extent and Chronology: A Closer Look, Developments in Quaternary Science*, v. 15. Elsevier, Amsterdam, 2011.

790 Etzelmüller, B., Guglielmin, M., Hauck, C., Hilbich, C. Hoelzle, M., Isaksen, K., Noetzli, J., Oliva, M., and Ramos, M.: Twenty years of European mountain permafrost dynamics—the PACE legacy, *Environ. Res. Lett.* 15, 104070, doi:10.1088/1748-9326/abae9d, 2020.

795 Eynaud, F., de Abreu, L., Voelker, A., Schönfeld, J., Salgueiro, E., Turon, J-L., Penaud, A., Toucanne, S., Naughton F., Sanchez Goñi, M.F., Malizé, B., and Cacho, I.: Position of the Polar Front along the western Iberian margin during key cold episodes of the last 45 ka, *Geochem. Geophys. Geosyst.*, 10, Q07U05, doi:10.1029/2009GC002398, 2009.

Fechtig H. and Kalbitzer S.: The diffusion of argon in potassium-bearing solids. In *Potassium–Argon Dating* (Eds. O. A. Schaeffer and J. Zinner), Springer, Heidelberg, 1966.

800 Fick, S.E., and Hijmans, R.J.: WorldClim 2: new 1-km spatial resolution climate surfaces for global land areas, *Int. J. Climatol.*, 37, 4302–4315, doi:10.1002/joc.5086, 2017.

Florineth, D., and Schlüchter, C.: Alpine evidence for atmospheric circulation patterns in Europe during the Last Glacial Maximum, *Quaternary Res.*, 54, 295–308, doi:10.1006/qres.2000.2169, 2000.

805

Ghadiri, E., Vogel, N., Brennwald, M.S., Maden, C., Häuselmann, A.D., Fleitmann, D., Cheng, H., and Kipfer, R.: Noble gas-based temperature reconstruction on a Swiss stalagmite from the last glacial–interglacial transition and its comparison with other climate records, *Earth Planet. Sci. Lett.*, 495, 192–201. doi:10.1016 /j.epsl.2018.05.019, 2018.



810 Ghadiri, E., Affolter, S., Brennwald, M.S., Fleitmann, D., Häuselmann, A.D., Cheng, H., Maden, C., Leuenberger, M., and
Kipfer, R.: Estimation of temperature – altitude gradients during the Pleistocene–Holocene transition from Swiss stalagmites,
Earth Planet. Sci. Lett., 544, 116387, doi: 10.1016/j.epsl.2020.116387, 2020.

Grämiger, L. M., Moore, J. R., Gischig, V. S., and Loew, S.: Thermomechanical stresses drive damage of Alpine valley rock
815 walls during repeat glacial cycles. *J. Geophys. Res.-Earth*, 123, 2620–2646, doi:10.1029/2018JF004626, 2018.

Gribenski, N., Valla, P.G., Preusser, F., Roattino, T., Crouzet, C., and Buoncristiani, J.-F.: Out-of-phase Late Pleistocene
glacial maxima in the Western Alps reflect past changes in North Atlantic atmospheric circulation. *Geology*, 49, 1096–1101,
doi:10.1130/G48688.1, 2021.

820

Gruber, S., Peter, M., Hoelzle, M., Woodhatch, I., and Haeblerli, W.: Surface temperatures in steep alpine rock faces: a strategy
for regional-scale measurement and modelling, *Proceedings of the 8th International Conference on Permafrost* (Eds. Arenson,
L.), Zürich, 325–330, 2003.

825 Gruber, S., Hoelzle, M., and Haeblerli, W.: Rock-wall temperatures in the Alps: modelling their topographic distribution and
regional differences, *Permafrost Periglac.*, 15, 299–307, doi:10.1002/ppp.501, 2004.

Guralnik, B., Tremblay, M.M., Phillips, M., Gribenski, N., Valla, P., and Hippe, K.: Cosmogenic ^3He - ^{10}Be - ^{14}C dating
quantifies Alpine climate response to global warming, *Goldschmidt Conference*, Boston, USA, 2018.

830

Haberkorn, A., Wever, N., Hoelzle, M., Phillips, M., Kenner, R., Bavay, M., and Lehning, M.: Distributed snow and rock
temperature modelling in steep rock walls using Alpine3D, *Cryosphere*, 11(1), 585–607, doi:10.5194/tc-11-585-2017, 2017.

Haeblerli, W., Huggel, C., Paul, F., and Zemp, M.: The response of glaciers to climate change: observations and impacts, In:
835 James, Allan; Harden, Carol; Clague, John. *Reference Module in Earth Systems and Environmental Sciences*, Elsevier, doi:
10.1016/B978-0-12-818234-5.00011-0, 2020.

Hallet, B.A.: Theoretical Model of Glacial Abrasion, *J. Glac.* 23, 39–50, doi:10.3189/S0022143000029725, 1979.

840 Harrison, T.M., and McDougall, I.: The thermal significance of potassium feldspar K–Ar ages inferred from $^{40}\text{Ar}/^{39}\text{Ar}$ age
spectrum results, *Geochim. Cosmochim. Ac.*, 46, 1811–1820, doi:10.1016/0016-7037(82)90120-X, 1982.



- Harrison, T.M., and Lovera, O.M.: The multi-diffusion domain model: past, present and future, Geological Society, London, Special Publications, 378, 91–106, doi:10.1144/SP378.9, 2013.
- 845
- Hasler, A., Gruber, S., and Haeberli, W.: Temperature variability and offset in steep alpine rock and ice faces, *The Cryosphere*, 5, 977–988, doi:10.5194/tc-5-977-2011, 2011.
- Heiri, O., Koinig, K.A., Spötl, C., Barrett, S., Brauer, A., Drescher-Schneider, R., Gaar, D., Ivy-Ochs, S., Kerschner, H.,
850 Luetscher, M., Moran, A., Nicolussi, K., Preusser, F., Schmidt, R., Schoeneich, P., Schwörer, C., Sprafke, T., Terhorst, B.,
and Tinner, W.: Palaeoclimate records 60–8 ka in the Austrian and Swiss Alps and their forelands, *Quaternary Sci. Rev.*, 106,
186–205, doi :10.1016/j.quascirev.2014.05.021, 2014a.
- Heiri, O., Brooks, S., Bedford, A., Hazekamp, M., Ilyashuk, B., Jeffers, E., Lang, B., Kirilova, E., Kuiper, S., Millet, L.,
855 Samartin, S., Tóth, M., Verbruggen, F., Watson, J., Asch, N., Renssen, H., Lammertsma, E., Birks, J., Birks, H., and Lotter,
A.: Validation of climate model-inferred regional temperature change for late-glacial Europe, *Nat. Commun.*, 5, 1–7,
doi:10.1038/ncomms5914, 2014b.
- Herman, F., De Doncker, F., Delaney, I., Prasicek, G., and Koppes, M.: The impact of glaciers on mountain erosion, *Nature*
860 *Rev. Earth Environ.*, 2 (6), 422–435, doi:10.1038/s43017-021-00165-9, 2021.
- Ivy-Ochs, S.: Glacier variations in the European Alps at the end of the last glaciation, *Cuad. Investig. Geografica*, 41, 295–
315, doi:10.18172/cig.2750, 2015.
- 865 Jaeger, J.M., and Koppes M.N: The role of the cryosphere in source-to-sink systems, *Earth-Sci. Rev.*, 153, 43–76,
doi:10.1016/j.earscirev.2015.09.011, 2016.
- Koppes, M., Hallet, B., Rignot, E., Mouginot, J., Wellner, J.S., and Boldt, K.: Observed latitudinal variations in erosion as a
function of glacier dynamics, *Nature*, 526, 100–103, doi:10.1038/nature15385, 2015.
- 870
- Kalashnikov, E., Tolstikhin, I., Lehmann, B., and Pevzner, B.: Helium transport along lattice channels in crystalline quartz, *J.*
Phys. Chem. Solids, 64, 2293–2300, doi:10.1016/S0022-3697(03)00264-6, 2003.
- Kapannusch, R., Scherler, D., King G., and Wu, H.: Glacial influence on late Pleistocene ¹⁰Be-derived paleo-erosion rates
875 in the north-western Himalaya, India, *Earth Planet. Sci. Lett.*, 547, 116441, doi:10.1016/j.epsl.2020.116441, 2020.



Kelly, M.A., Ivy-Ochs, S., Kubik, P., von Blanckenburg, F., and Schlüchter, C.: Chronology of deglaciation based on ^{10}Be dates of glacial erosional features in the Grimsel Pass region, central Swiss Alps, *Boreas*, 35, 634–643, doi:10.1080/03009480600690829, 2006.

880

Kerschner, H., and Ivy-Ochs, S.: Palaeoclimate from glaciers: examples from the Eastern Alps during the Alpine Lateglacial and early Holocene, *Global Planet. Change*, 60, 58–71, doi:10.1016/j.gloplacha.2006.07.034, 2008.

Kerschner, H., Kaser, G., and Sailer, R.: Alpine Younger Dryas glaciers as paleo-precipitation gauges, *Ann. Glaciol.*, 31, 80–84, doi:10.3189/172756400781820237, 2000.

885

Kuhlemann, J., Rohling, E.J., Krumrei, I., Kubik, I., Ivy-Ochs, S., Kucera, M.: Regional synthesis of Mediterranean atmospheric circulation during the Last Glacial Maximum, *Science*, 321, 1338–1340, doi:10.1126/science.1157638, 2008.

Labhart, TP.: Aarmassiv und Gotthardmassiv, G. Fischer Verlag, Stuttgart, 1977.

890

Lee, J. K. W.: Multipath diffusion in geochronology, *Contrib. Mineral. Petr.*, 120, 60–82, doi:10.1007/BF00311008, 1995.

Lehmann, B., Herman, F., Valla, P.G., King, G.E., Biswas, R.H., Ivy-Ochs, S., Steinemann, O., and Christl, M.: Postglacial erosion of bedrock surfaces and deglaciation timing: New insights from the Mont Blanc massif (western Alps), *Geology*, 48, 139–144, doi:10.1130/G46585.1, 2020.

895

Li, H., Spötl, C., and Cheng, H.: A high-resolution speleothem proxy record of the Late Glacial in the European Alps: extending the NALPS19 record until the beginning of the Holocene, *J. Quat. Sci.*, 36, 29–39, doi:10.1002/jqs.3255, 2021.

900 Lin, K.J., Ding, H., and Demkowicz, M.J.: Formation, migration, and clustering energies of interstitial He in α -quartz and β -cristobalite, *J. Nucl. Mater.*, 479, 224–231, doi:10.1016/j.jnucmat.2016.06.049, 2016.

Lingling, L., Lingling, W., Shuchen, L., Yaochun, Y., Hua, T., Fengxia, S., Chaowen, X., Lei, L., Yi, L., Yueju, C., Ying, L., and Jijun, X.: A first-principles study of helium diffusion in quartz and coesite under high pressure up to 12GPa, *Geosci. Front.*, 12(2), 1001–1009, doi:10.1016/j.gsf.2020.09.009, 2021.

905

Lovera, O.M., Richter, F.M., and Harrison, T.M.: The $^{40}\text{Ar}/^{39}\text{Ar}$ thermochronometry for slowly cooled samples having a distribution of diffusion domain sizes, *J. Geophys. Res.*, 94, 17917–17935, doi:10.1029/JB094iB12p17917, 1989.



910 Lovera, O.M., Richter, F.M., and Harrison, T. M.: Diffusion domains determined by ^{39}Ar release during step heating, *J. Geophys. Res.*, 96, 2057–2069, doi:10.1029/90JB02217, 1991.

Lovera, O.M., Grove, M., and Harrison, T.M.: Systematic analysis of K-feldspar $^{40}\text{Ar}/^{39}\text{Ar}$ step-heating experiments II: relevance of laboratory K-feldspar argon diffusion properties to Nature, *Geochim. Cosmochim. Ac.*, 66, 1237–1255,
915 doi:10.1016/S0016-7037(01)00846-8, 2002.

Luetscher, M., Boch, R., Sodemann, H., Spötl, C., Cheng, H., Edwards, R. L., Frisia, S., Hof, F., and Müller, W.: North Atlantic storm track changes during the Last Glacial Maximum recorded by Alpine speleothems, *Nature Comm.*, 6, 6344,
doi:10.1038/ncomms7344, 2015.

920

Magnin, F., Brenning, A., Bodin, X., Deline, P., and Ravel, L.: Statistical modelling of rock wall permafrost distribution: application to the Mont Blanc massif, *Geomorphologie*, 21, 145–162, doi:10.4000/geomorphologie.10965, 2015a.


Magnin, F., Deline, P., Ravel, L., Noetzli, J., and Pogliotti, P.: Thermal characteristics of permafrost in the steep alpine rock
925 walls of the Aiguille du Midi (Mont Blanc Massif, 3842m a.s.l), *The Cryosphere*, 9, 109–121, doi:10.5194/tc-9-109-201,
2015b.

Magnin, F., Josnin, J.-Y., Ravel, L., Pergaud, J., Pohl, B., and Deline, P.: Modelling rock wall permafrost degradation in the
Mont Blanc massif from the LIA to the end of the 21st century, *The Cryosphere*, 11, 1813–1834, doi:10.5194/tc-11-1813-
930 2017, 2017.

Magny, M., Guiot, J., and Schoellammer, P.: Quantitative Reconstruction of Younger Dryas to Mid-Holocene Paleoclimates
at Le Locle, Swiss Jura, Using Pollen and Lake-Level Data, *Quaternary Res.*, 56(2), doi:10.1006/qres.2001.2257, 170–180,
2001.

935

Mair, D., Lechmann, A., Delunel, R., Yesilyurt, S., Tikhomirov, D., Vockenhuber, C., Christl, M., Akçar, N., and Schlunegger,
F.: The role of frost cracking in local denudation of steep Alpine rockwalls over millennia (Eiger, Switzerland), *Earth Surf.
Dynam.*, 8, 637–659, doi:10.5194/esurf-8-637-2020, 2020.

940 Mariotti, A., Blard , Charreau, J., Toucanne, S., Jorry, S.J., Molliex, S., Bourlès, D.L., Aumaître, G., and Keddadouche,
K.: Nonlinear forcing of climate on mountain denudation during glaciations, *Nat. Geosci.*, 14, 16–22, doi:10.1038/s41561-
020-00672-2, 2021.



945 Martin, L.C.P., Blard, P.H., Lavé, J., Jomelli, V., Charreau, J., Condom, T., Lupker, M., and ASTER Team: Antarctic-like temperature variations in the Tropical Andes recorded by glaciers and lakes during the last deglaciation, *Quaternary Sci. Rev.*, 247, 106542, doi:10.1016/j.quascirev.2020.106542, 2020.

Masarik, J., and Reedy, R.C.: Monte Carlo simulation of the in-situ-produced cosmogenic nuclides, *Radiocarbon*, 38, 163, <http://206.189.126.38:8081/index.php/radiocarbon/article/view/1890>, 1996.

950

Monegato, G., Scardia, G., Hajdas, I., Rizzini, F., and Piccin, A.: The Alpine LGM in the boreal ice-sheets game, *Nature Sci. reports*, 7, 2078, doi:10.1038/s41598-017-02148-7, 2017.

955 Moseley, G.E., Spötl, C., Brandstätter, S., Erhardt, T., Luetscher, M., and Edwards, R.L.: NALPS19: sub-orbital-scale climate variability recorded in northern Alpine speleothems during the last glacial period, *Climate of the Past*, 16, 29–50, doi:10.5194/cp-16-29-2020, 2020.

NGRIP members: High-resolution record of Northern Hemisphere climate extending into the last interglacial period, *Nature*, 43, 147–151, doi:10.1038/nature02805, 2004.

960

Nichols, K.A., and Goehring, B.: Isolation of quartz for cosmogenic in situ ^{10}Be analysis, *Geochronology*, 1, 43–52, doi:10.5194/gchron-1-43-2019, 2019.

965 Peyron, O., Guiot, J., Cheddadi, R., Tarasov, P., Reille, M., de Beaulieu, J.-L., Bottema, S., and Andrieu, V.: Climatic Reconstruction in Europe for 18,000 YR B.P. from Pollen Data, *Quaternary Res.*, 49(2), 183–196, doi:10.1006/qres.1997.1961, 1998.

970 Protin, M., Schimmelpfennig, I., Mugnier, J-L., Ravanel, L., Le Roy, M., Deline, P., Favier, V., and Buoncristiani, J-F.: Climatic reconstruction for the Younger Dryas/Early Holocene transition and the Little Ice Age based on paleo-extents of Argentière glacier (French Alps), *Quaternary Sci. Rev.*, 221, 105863, doi:10.1016/j.quascirev.2019.105863, 2019.

Prud'homme, C., Vassallo, R., Crouzet, C., Cracaillet, J., Mugnier, J-L., and Cortès-Aranda, J.: Paired ^{10}Be sampling of polished bedrock and erratic boulders to improve dating of glacial landforms: an example from the Western Alps, *Earth Surf. Proc. Land.*, 45, 1168–1180, doi:10.1002/esp.4790, 2020.

975



- Reddy, S.M., Potts, G.J., Kelley, S.P., and Arnaud, N.O.: The effects of deformation-induced microstructures on intragrain $^{40}\text{Ar}/^{39}\text{Ar}$ ages in potassium feldspar, *Geology*, 27, 363–366, doi:10.1130/0091-7613(1999)027<0363:TEODIM>2.3.CO;2, 1999.
- 980 Reiners, P.W., Ehlers, T.A., and Zeitler, P.K.: Past, Present, and Future of Thermochronology, *Rev. Mineral. Geochem.*, 58, 1–18, doi:10.2138/rmg.2005.58.1, 2005.
- Schaltegger, U., and Krähenbühl, U.: Heavy rare-earth element enrichment in granites of the Aar Massif (Central Alps, Switzerland), *Chemical Geology*, 89, 49–63, doi: 10.1016/0009-2541(90)90059-G, 1990.
- 985
- Seguinot, J., Ivy-Ochs, S., Juvet, G., Huss, M., Funk, M., and Preusser, F.: Modelling last glacial cycle ice dynamics in the Alps, *The Cryosphere*, 12, 3265–3285, doi:10.5194/tc-12-3265, 2018.
- Seltzer, A.M., Ng, J., Aeschbach, W., Kipfer, R., Kulongoski, J.T., Severinghaus, J.P., and Stute, M.: Widespread six degrees Celsius cooling on land during the Last Glacial Maximum, *Nature*, 593, 228–232, doi:10.1038/s41586-021-03467-6, 2021.
- 990
- Shuster, D.L., and Farley, K.A.: Diffusion kinetics of proton induced ^{21}Ne , ^3He , and ^4He in quartz, *Geochim. Cosmochim. Ac.*, 69, 2349–2359, doi:10.1016/j.gca.2004.11.002, 2005.
- Shuster, D.L., Farley, K.A., Sistierson, J.M., and Burnett D.S.: Quantifying the diffusion kinetics and spatial distributions of radiogenic ^4He in minerals containing proton-induced ^3He , *Earth Planet. Sci. Lett.*, 217, 19–32, doi:10.1016/S0012-821X(03)00594-6, 2004.
- 995
- Stone, J.O.: Air pressure and cosmogenic isotope production, *J. Geophys. Res.*, 105, 753–759, doi:10.1029/2000JB900181, 2000.
- 1000
- Tremblay, M.M., Shuster D.L., and Balco, G.: Cosmogenic noble gas paleothermometry, *Earth Planet. Sci. Lett.*, 400, 195–205, doi:10.1016/j.epsl.2014.05.040, 2014a.
- Tremblay, M.M., Shuster, D.L., and Balco, G.: Diffusion Kinetics of ^3He and ^{21}Ne in Quartz and Implications for Cosmogenic Noble Gas Paleothermometry, *Geochim. Cosmochim. Ac.*, 142, 186–204, doi:10.1016/j.gca.2014.08.010, 2014b.
- 1005
- Tremblay, M., Shuster, D., Spagnolo, M., Renssen, H., and Ribolini, A.: Temperatures recorded by cosmogenic noble gases since the last glacial maximum in the Maritime Alps, *Quaternary Res.*, 91(2), 829–847, doi:10.1017/qua.2018.109, 2018.



1010 Trumbly, M.: ThermoChronology-At-Purdue/Gribenski2022: Gribenski2022_submissionv1.0.0 (v1.0.0), Zenodo [code],
1015 <https://doi.org/10.5281/zenodo.5808021>, 2021.

Vermeesch, P., Baur, H., Heber, V.S., Kober, F., Oberholzer, P., Schaefer, J.M., Schlüchter, C., Strasky, S., and Wieler, R.:
Cosmogenic ^3He and ^{21}Ne measured in quartz targets after one year of exposure in the Swiss Alps, *Earth Planet. Sci. Lett.*,
1015 284, 417–425, doi:10.1016/j.epsl.2009.05.007, 2009.

Višnjević, V., Herman, F., and Prasicek, G.: Climatic patterns over the European Alps during the LGM derived from inversion
of the paleo-ice extent, *Earth Planet. Sci. Lett.*, 538, 116185, doi:10.1016/j.epsl.2020.116185, 2020.

1020 Wirsig, C., Zasadni, J., Christl, M., Akçar, N., and Ivy-Ochs, S.: Dating the onset of LGM ice surface lowering in the High
Alps. *Quaternary Sci. Rev.*, 143, 37–50, doi:10.1016/j.quascirev.2016.05.001, 2016a.

Wirsig, C., Zasadni, J., Ivy-Ochs, S., Christl, M., Kober, F., and Schlüchter, C.: A deglaciation model of the Oberhasli,
Switzerland, *J. Quat. Sci.*, 31, 46–59, doi:10.1002/jqs.2831, 2016b.

1025

Wu, H. B., Guiot, J. L., Brewer, S., and Guo, Z. T.: Climatic changes in Eurasia and Africa at the last glacial maximum and
mid-Holocene: reconstruction from pollen data using inverse vegetation modelling, *Clim. Dynam.*, 29, 211–229,
doi:10.1007/s00382-007-0231-3, 2007.

1030 Zemp, M., Haeberli, W., Hoelzle, M., and Paul, F.: Alpine glaciers to disappear within decades? *Geophys. Res. Lett.*, 33,
L13504, doi:10.1029/2006GL026319, 2006.

Cosmogenic ^3He paleothermometry on post-LGM glacial bedrock within the central European Alps

Natacha Gribenski, Marissa M. Tremblay, Pierre G. Valla, Greg Balco, Benny Guralnik, David L. Shuster

Data supplementary

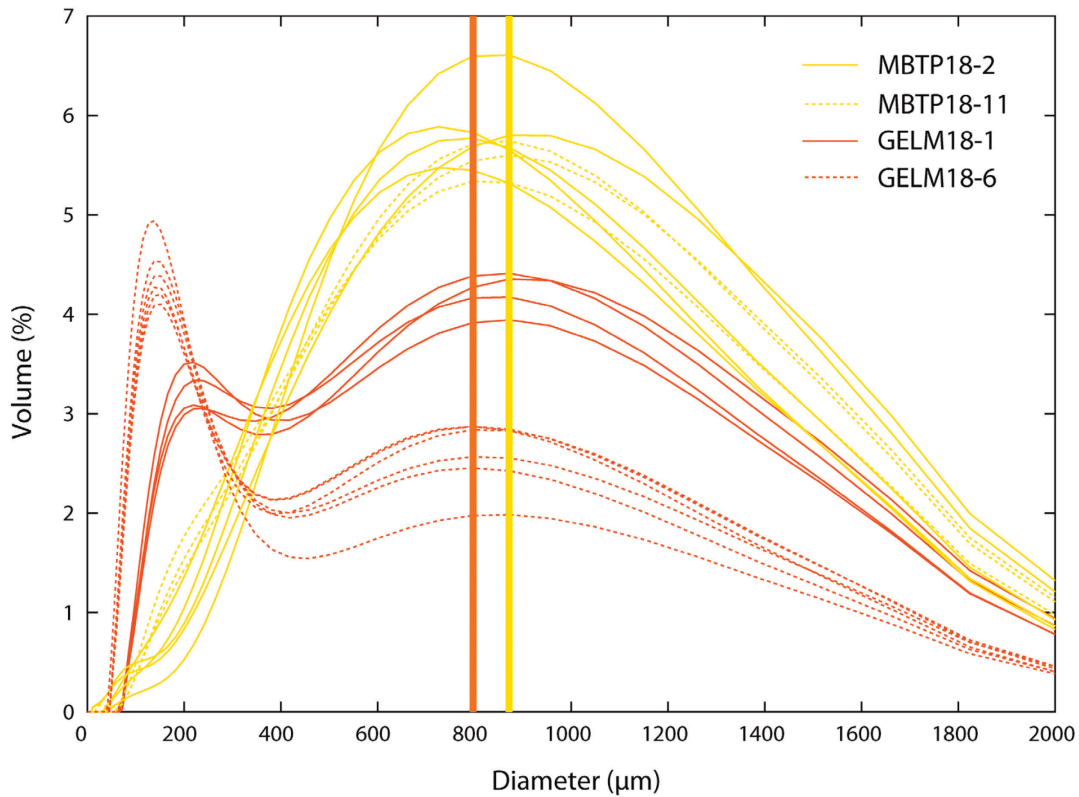


Figure S1: Grain-size distribution measured using laser diffraction after *Selfrag* crushing (fraction ≤ 1.5 mm) for two representative samples per study site: MBTP (MBTP18-2, -11) and GELM (GELM18-01, -06). Multiple lines represent replicates for each sample. Thick vertical lines indicate the averaged mode for the MBTP (yellow line) and the GELM (orange line) sites, when excluding the finer fraction (i.e. <200 μm).

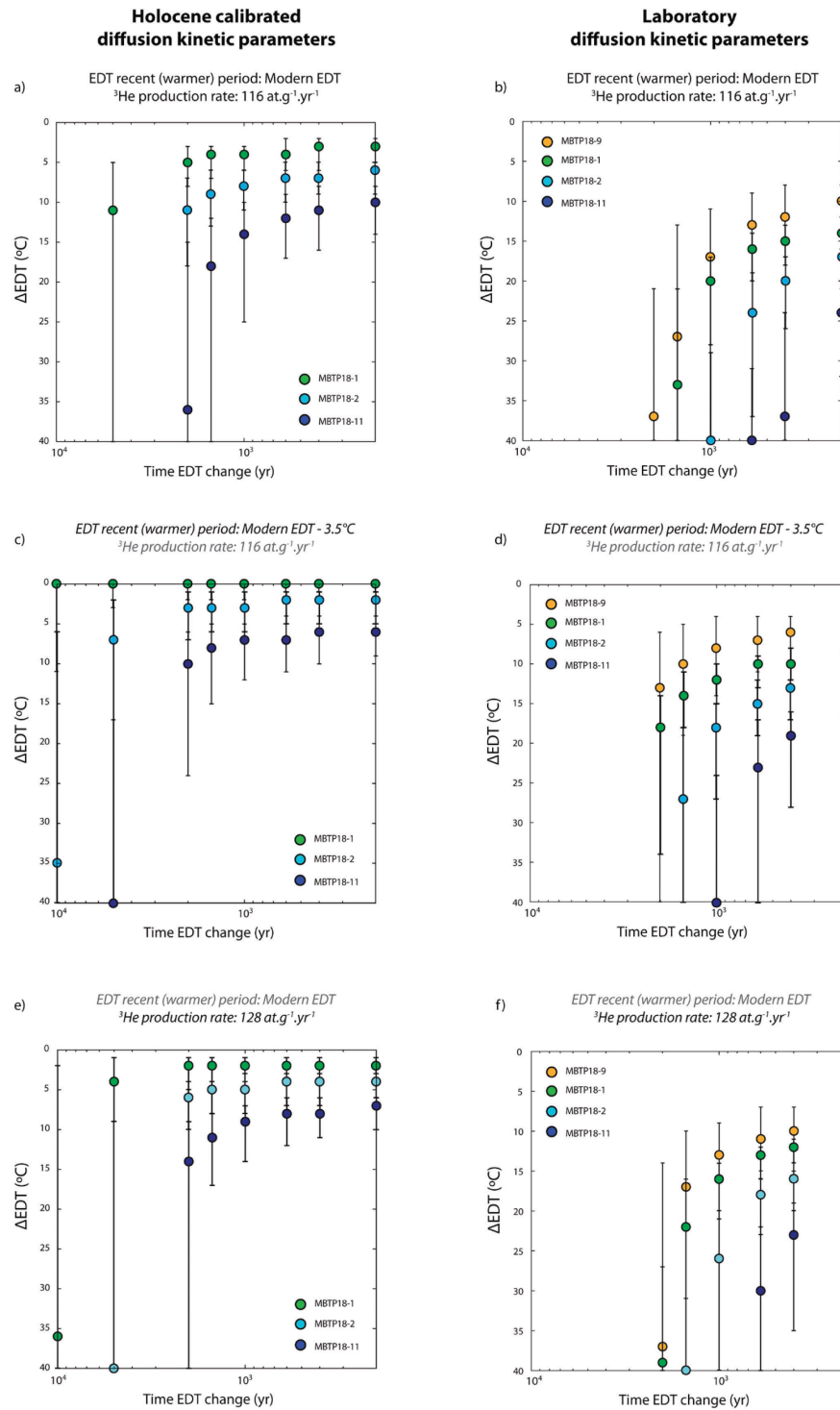


Figure S2: ΔEDT solutions as function of time of EDT change from time-varying EDT forward simulations conducted using MBTP diffusion kinetics calibrated with Holocene samples (left panels) or solely based on laboratory experiments (right panels), with a) and b): recent EDT equal to the Modern EDT and using a ^3He production rate of $116 \text{ at.g}^{-1}.\text{yr}^{-1}$; c) and d): recent EDT equal to the Modern EDT minus 3.5°C ; e) and f): ^3He production increased by 10% ($128 \text{ at.g}^{-1}.\text{yr}^{-1}$).

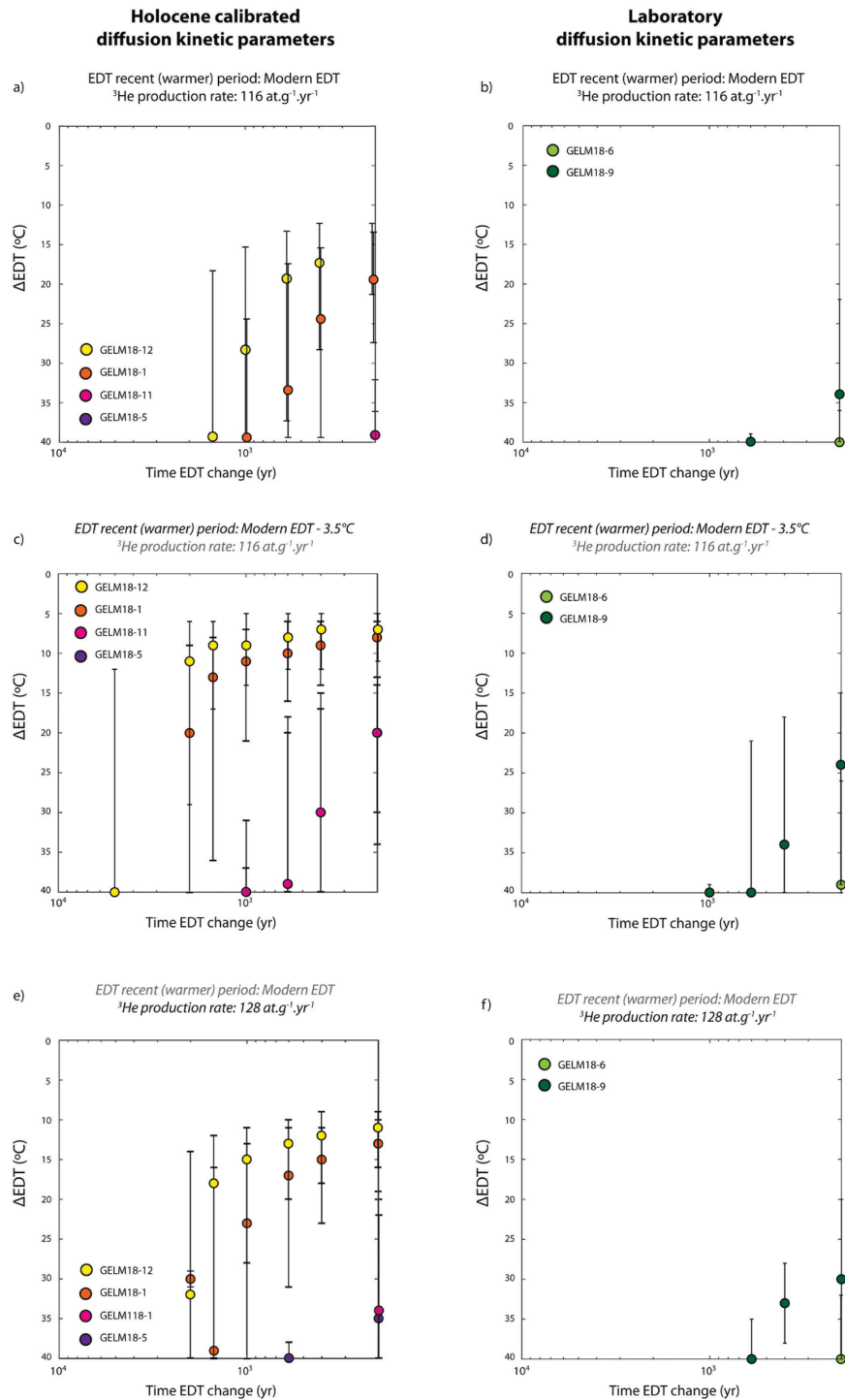


Figure S3: ΔEDT solutions as function of time of EDT change from time-varying EDT forward simulations conducted using GELM diffusion kinetics calibrated with Holocene samples (left panels) or solely based on laboratory experiments (right panels), with a) and b): recent EDT equal to the Modern EDT and using a ^3He production rate of $116 \text{ at.g}^{-1}.\text{yr}^{-1}$; c) and d): recent EDT equal to the Modern EDT minus 3.5°C ; e) and f): ^3He production increased by 10% ($128 \text{ at.g}^{-1}.\text{yr}^{-1}$). Only solutions for Holocene samples (GELM18-6 and -9) exist when using diffusion kinetics parameters solely based on laboratory experiments.

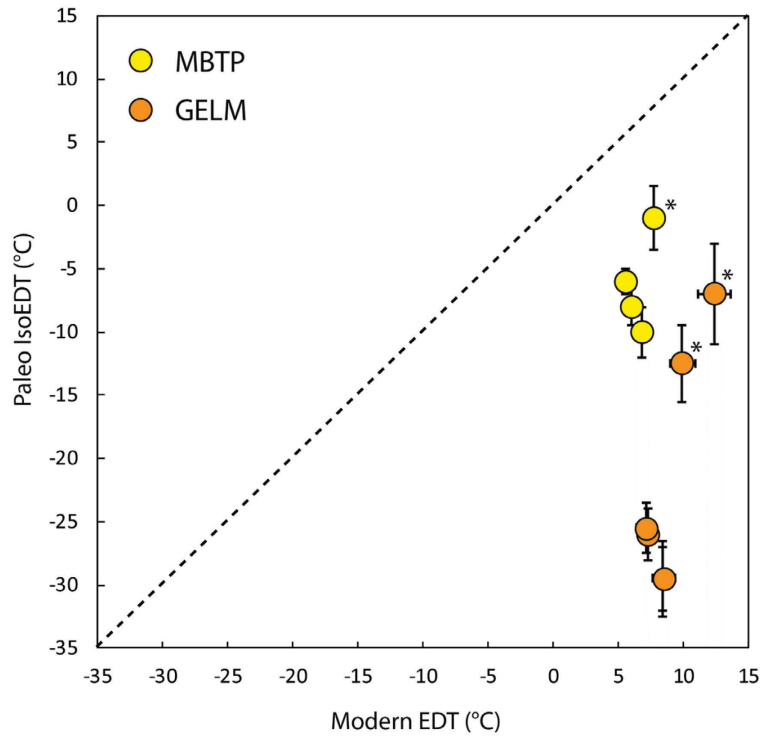


Figure S4: Comparison of modern EDTs and paleoIsoEDTs obtained using diffusion kinetics from laboratory experiments (without Holocene calibration), for both MBTP and GELM samples. The asterisks indicate the Holocene samples.

Table S1: ³He step-degassing experiment data for MBTP18-9.

Step	Time (minutes)	Temperature (°C)	³ He (x10 ⁴ at.) ¹	±1σ (x10 ⁴ at.)
1	60	100.0	4545.5	2.9
2	120	100.0	4490.0	2.7
3	80	70.0	159.3	1.3
4	160	70.0	294.0	1.4
5	240	70.0	412.6	1.4
6	120	90.0	1071.6	1.8
7	180	90.0	1518.8	1.8
8	180	100.0	2468.7	2.4
9	60	120.0	2819.5	2.2
10	120	120.0	3925.4	2.5
11	180	120.0	3763.1	2.8
12	60	140.0	3763.9	2.7
13	120	140.0	5053.9	3.2
14	180	140.0	5802.7	3.0
15	60	160.0	5143.1	3.0
16	120	160.0	8313.4	3.5
17	180	160.0	7663.2	3.8
18	60	180.0	7649.0	3.4
19	120	180.0	11902.7	4.8
20	180	180.0	12152.2	4.7
21	60	200.0	8488.6	4.0
22	120	200.0	10957.0	4.7
23	180	200.0	8829.8	4.1
24	30	249.9	7760.8	3.8
25	60	250.0	4271.1	2.7
26	30	299.9	2572.0	2.2
27	60	300.0	919.9	1.7
28	30	324.9	209.0	1.3
29	60	324.9	64.6	1.3
30	30	349.9	7.3	1.2
31	60	349.9	-0.1	1.2
32	60	334.9	-0.9	1.2
33	60	310.0	-4.7	1.2
34	90	290.0	0.6	1.2
35	90	250.0	-1.8	1.2
36	120	250.0	-0.7	1.2
37	180	215.0	-1.1	1.2
38	120	265.0	1.0	1.2
39	90	285.0	1.0	1.2
40	60	299.9	-1.7	1.2
41	60	330.0	-0.8	1.2
42	60	359.9	2.6	1.2
43	60	379.9	-2.3	1.2
44	30	399.9	7.9	1.2
45	60	399.9	0.1	1.2
46	30	424.9	0.5	1.2
47	60	424.9	0.4	1.2
48	30	449.9	-0.5	1.2
49	60	449.9	-2.3	1.2
50	30	474.9	-1.3	1.2

51	60	474.9	-0.1	1.2
52	30	499.9	-0.1	1.2
53	30	549.9	0.8	1.2

¹Measurements of ³He were made on a quartz grain of 700 μ m spherical equivalent diameter and all ³He abundances were background corrected using an averaged room temperature blank of $2.1 \pm 1.2 \times 10^4$ at.

Heating steps in gray were excluded from MDD models (Figure 3a) because measured ³He abundances are below or close to below the detection level.

Table S2: ³He step-degassing experiment data for GELM18-1.

Step	Time (minutes)	Temperature (°C)	³ He (x10 ⁴ at.) ¹	$\pm 1\sigma$ (x10 ⁴ at.)
1	60	100.04	21022.5	58.7
2	120	99.99	2616.0	21.3
3	80	69.99	134.7	7.3
4	160	69.99	226.1	7.7
5	240	70	263.6	8.3
6	120	89.99	584.8	12.0
7	180	89.98	664.6	11.8
8	180	99.99	1852.6	22.8
9	60	119.97	3044.8	23.7
10	120	119.98	3754.4	26.2
11	180	119.99	3218.5	25.1
12	60	139.95	3080.2	23.9
13	120	139.98	2976.3	25.3
14	180	139.98	3045.7	21.2
15	60	159.96	2171.2	23.3
16	120	159.98	4880.1	26.7
17	180	159.98	3679.0	24.0
18	60	179.96	2683.4	19.7
19	120	179.98	4284.9	28.4
20	180	179.99	3833.4	22.4
21	60	199.96	2037.0	19.6
22	120	199.98	2328.3	19.4
23	180	199.98	1963.4	19.1
24	30	249.89	1769.6	16.4
25	60	249.94	2248.4	20.2
26	30	299.67	4103.9	22.9
27	60	300.0	-1.5	5.1
28	30	325.1	-4.7	5.0
29	30	499.9	9.0	5.2

¹ Diffusion kinetics ³He measurements were made on a quartz grain of 900 μ m spherical equivalent diameter and all ³He abundances were background corrected using an averaged room temperature blank of $4.8 \pm 4.8 \times 10^4$ at.

Heating steps in gray were excluded from MDD models (Figure 3b) because measured ³He abundances are below or close to below the detection level.

Table S3: Measured ^{10}Be and ^3He concentrations.

Sample	Lat./Long. (°N/°E)	Alt. (asl)	Thick. (^{10}Be , cm) ¹	Shield. ¹	^{10}Be conc. (at.g ⁻¹) ¹	±1σ	^3He conc. (at.g ⁻¹) ²	±1σ
MBTP18-1	45.9083/6.9311	2460	8	0.963	474750	600	6396493	520929
MBTP18-2	45.9086/6.9319	2133	8.5	0.949	403210	600	6327725	508608
MBTP18-9	45.9124/6.933	2310	6	0.656	160300	500	1872439	328634
MBTP18-11	45.9108/6.9315	2387	7	0.898	330490	500	5773930	505672
GELM18-1	46.6218/8.3257	2155	1	0.977	458000	1200	5445078	504014
GELM18-5	46.6185/8.3215	1888	4	0.934	173000	800	1246347	231974
GELM18-6	46.6151/8.3212	1418	1	0.949	139000	1000	642092	247299
GELM18-9	46.6136/8.3071	2154	1	0.986	317000	900	4589051	399870
GELM18-11	46.6221/8.3258	2402	2.5	0.929	567000	1500	6153719	624435

¹Reported from Lehmann et al. (2020; MBTP site) and Wirsig et al. (2016b; GELM site). ²All samples for ^3He were collected at less than 3 cm depth, and mean ^3He concentrations from three replicate measurements (Table S2; 400-500 μm radii fraction) per sample were used as final ^3He concentrations.

Table S4: Detail of replicate measurements of ^3He concentrations.

Sample	Replicate	Mass (g)	^3He conc. (at.g ⁻¹) ¹	±1σ
MBTP18-1	a	0.108	5994723	523769
	b	0.087	6725368	611132
	c	0.109	6469388	427888
MBTP18-2	a	0.097	6917377	571202
	b	0.095	6558617	561876
	c	0.127	5507182	392741
MBTP18-9	a	0.103	1593779	318411
	b	0.096	1905925	346033
	c	0.115	2117615	321458
MBTP18-11	a	0.106	6308056	526209
	b	0.075	5372795	587753
	c	0.130	5640938	403056
GELM18-1	a	0.097	5760774	491090
	b	0.093	4629382	528326
	c	0.094	5945078	492625
GELM18-5	a	0.101	4487736	541743
	b	0.083	3500198	458624
	c	0.097	5361562	449200
GELM18-6	a	0.111	1366551	241982
	b	0.122	1191473	231274
	c	0.121	1181018	222666
GELM18-9	a	0.086	535331	285142
	b	0.122	728596	236666
	c	0.130	662351	220088
GELM18-11	a	0.119	4680068	416420
	b	0.125	3654077	366976
	c	0.102	5433011	416215
GELM18-12	a	0.057	6002823	842018
	b	0.091	6092740	599051
	c	0.128	6365596	432235

¹ ^3He concentration measurements were made on the 400-500 μm radii fraction, applying an analytical blank correction of 7.7×10^3 atoms.